Università degli Studi di Padova

Dipartimento di Fisica e Astronomia "Galileo Galilei"

Corso di Laurea Magistrale in Astronomia

Binarity as a possible explanation of the dual horizontal branch in NGC 6791

Relatore
Dr. Giovanni Carraro

Controrelatore
Dr. Anna Marino
Università di Padova

Laureando
Varun M. Chaturmutha
Matricola: 1183476

Academic Year 2018/2019

Dedicated to those close to my heart..

Abstract

NGC 6791 is quite a famous old open cluster which harbors a dual red giant clump. A classical red clump, made of 45 stars, and a very blue clump (extended horizontal branch (EHB)), made of 12 stars. The origin of the second clump, composed of stars with virtually no envelope, is still disputed. Briefly, the lack of envelope is ascribed either to mass loss during the RGB phase, enhanced by the high cluster metallicity, or by binary evolution, and mass loss during the common envelope phase. It is crucial therefore to measure in a robust way the binary fraction of the cluster, especially for stars in the RGB phase. We will derive this percentage from a multi-epoch spectroscopic campaign conducted with FLAMES @ VLT. The plan of the thesis is to derive binary percentage through radial velocity distribution, and hence realize the possibility of binarity being the source for the formation of EHB stars.

Contents

Listing of figures

Listing of tables

The nitrogen in our DNA, the calcium in our teeth, the iron in our blood, the carbon in our apple pies were made in the interiors of collapsing stars. We are made of starstuff.

Carl Sagan

1

Introduction

IMAGINE AN ALIEN POPULATION, that gets to study *a* human being for ten minutes. What would be the extent of the conclusions they can draw from that human being? They could easily say about the presence of a periodic beat, a red fluid, and a continuous breathing pattern, among some more superficial deductions. But they would not be able to tell one of the most important characteristic of a human: *the process of aging*. Only if they can study more humans at a time, they would be able to assert that humans are born and eventually die. In the case of stars, we are the aliens trying to understand them. Studying their evolution has been possible due to the presence of many stars, in different evolutionary stages at any given time.

A star cluster can have from hundreds to over thousands of stars, each of which is at a unique stage in their evolution. Another very important idea that will be employed is that every old star was young at some stage of their life, with similar properties to stars that are currently in their youth.

In this Master‘s Thesis, we will exploit these ideas to understand the presence of the dual horizontal branch in the open cluster NGC 6791. A dual horizontal branch is comprised

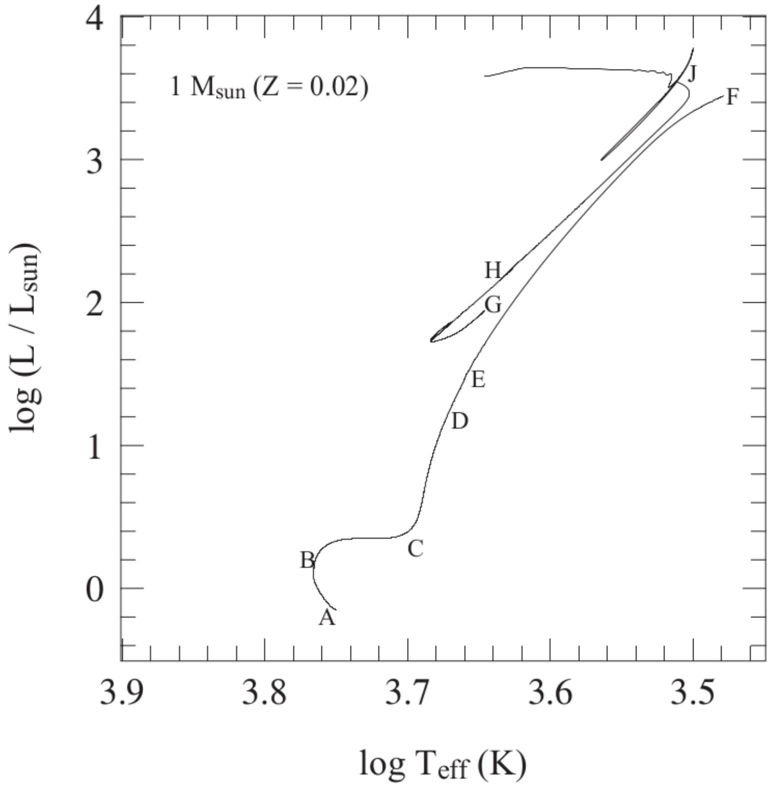

Figure 1.1: Evolution of a $1M_{\odot}$ star of initial composition X=0.7, Z=0.02. The letters A...J indicate corresponding points in the evolution track in the (Hertzsprung-Russell) H-R diagram.

of an extended horizontal branch (EHB) and a red clump (RC). The EHB stars have a very thin envelope. This lack of an envelope is a result of an increased mass loss in the post-main sequence evolutionary phases. Before we engage ourselves further into understanding the causes, let us discuss about the different components involved in the problem.

1.1 Stellar Evolution

A star is born out of interstellar (molecular) gas cloud, survives on its internal energy supply for a certain amount of time, and dies eventually after this supply is exhausted. Between the birth and death of a star, it goes through various evolutionary phases. These phases are characterized based on the fuel it is utilizing. For our discourse, we shall discuss the evolution of low mass stars ($M < 2M_{\odot}$).

A newly forming star from collapsing clouds needs to reach high density and temperature at the core to initiate nuclear burning. In the early stages of this collapse, the star is very cool for this burning. The source of energy for its luminosity at this stage is gravitational contraction. Once the star reaches high enough temperatures and densities at the center, hydrogen starts to undergo nuclear fusion. The energy produced by this nuclear fusion now replaces gravitational contraction as the source of energy for its luminosity. The photons trying to escape the stellar interiors counters against the gravitational collapse and bring the star into a hydrostatic equilibrium. It is at this stage that when the star is in hydrostatic equilibrium, it has reached the Main Sequence (MS) which is shown by point A in figure 1.1. X is the mass fraction of hydrogen, Y is the mass fraction of helium, and Z is the fraction of metals (all elements other than hydrogen and helium).

For a solar mass star, the hydrogen burning stage lasts for $\sim 10^{10}$yr. Hydrogen burning produces helium, which starts forming the central core of the star. The core is yet not hot enough to start helium burning while hydrogen burning is still active in the central core. Hydrogen is almost exhausted at point B ($X_{core} = 10^{-3}$) after 9 Gyr, following which energy generation is gradually shifted to a thick hydrogen shell surrounding the freshly formed helium core. The hydrogen burning in the shell feeds the helium core hence gaining in mass. The helium core contracts rapidly and heats up, while the shell surrounding the core continues to burn hydrogen. The increasing mass and contraction of the helium core makes it so dense, that it becomes degenerate by point C. At this stage it finds itself at the base of the red giant branch. The degenerate gas pressure depends only on the density and not on the temperature. Hence even with an increasing temperature and density, the core reaches very high degenerate pressure owing to independence over temperature. This degenerate pressure is soon sufficient to balance all the upper layers of gas even without any ongoing fusion reaction in the core. With the contraction of the core, the envelope expands and cools and the star inflates to become a red giant. The temperatures are yet not high enough for helium fusion. As the star ascends up the red giant branch (point C onwards), the outer convective envelope starts to deepen. At point D, the convective envelope reaches its deepest extent to the layers that processed H-burning during the MS.

From point C, the star begins its climb up the red giant branch. On this journey, the stellar luminosity increases along with the stellar radius. This in turn means the envelope is getting loosely bound by gravity and it becomes easier for photon flux to remove mass from the stellar surface. The process driving mass loss in red giants is not very well understood as yet. The effect of mass loss can be calculated approximately based on the empirical formula by Reimers (Reimers, 1975):

$$\dot{M} = -4 \times 10^{-13} \eta \frac{L}{L_\odot} \sqrt{\frac{M_\odot}{M} \frac{g_\odot}{g}} M_\odot / yr \tag{1.1}$$

where $\dot{M}$ is the mass loss rate in solar units, M is the mass, L is the luminosity, and g is the surface gravity of the star. $\odot$ symbolizes solar values. η is the Reimers' stellar wind mass loss parameter and has a value of about $0.25 - 0.5$.

As the star ascends the RGB, at the tip of the RGB (at point F), the core mass is $\approx 0.45 M_\odot$, and $L = 2000 L_\odot$, the temperature of the helium core has reached $\approx 10^8$K with a core density $\approx 10^6$gcm^{-3}. Although this temperature is sufficient for helium fusion by the triple alpha (3α) process, the fusion is unstable under these conditions as the helium core is strongly degenerate. The energy that is generated by the 3α increases the temperature of the core and initiates a thermonuclear runaway (or the helium flash). During the helium flash, for a brief time, large quantities of helium are converted into carbon through the 3α process. Once the degeneracy in the helium core is lifted, helium burning becomes stable and the star moves to the zero age horizontal branch at point G. Along with an helium burning core, there is also a surrounding hydrogen burning shell.

The stars between point G and point H, form the horizontal branch (HB). Independent of their exact age or composition, the stars in the HB end up having about the same absolute luminosity. This is why they tend to "clump" in a particular spot in the color-magnitude diagram (figure 1.2; T= 5000K & L=75 L$_\odot$) and what makes them standard candles: The apparent brightness of RC stars is directly related to their distance. Once helium burning is exhausted in the core, the star begins to grow rapidly in radius and cools. The star follows an almost parallel path to the earlier RGB ascend, only with a slightly higher effective temperature. At this stage of evolution, the star has a contracting carbon-oxygen (C-O) core, a helium burning shell outside the C-O core, and a hydrogen burning shell outside the helium burning shell. Helium burning via the 3α fusion is very sensitive to temperature and the fusion rate goes by $\sim$ T^{40}. Hence, small changes in temperature result in large changes in energy output. The star hence experiences huge thermal pulses which destabilizes the outer envelope. This results in a slow ejection of the outer envelope. The C-O core continues to contract, but never reaches the carbon fusion temperature ($\sim 6 \times 10^8$K). As the envelope is ejected, the star becomes host to a planetary nebula. The C-O core is now exposed with no constant energy source to maintain a hydrostatic equilibrium. This core continues to contract and the star rapidly move towards higher effective temperatures after point J at a nearly constant luminosity. The C-O core then hits the critical density where the gas becomes degenerate. The pressure now becomes independent of temperature, and it grows rapidly to counteract the gravitation collapse of the C-O core. This degenerate core becomes a White Dwarf.

1.2 OPEN CLUSTERS

Open clusters are a group of a few hundred to thousand stars that are loosely bound by gravity. They are named so due to the fact that individual stars can be resolved easily through a telescope. These clusters are located in dusty spiral arms and irregular galaxies, that show active star formation. They usually survive for a few hundred million years, while more massive ones may survive for longer. NGC 6791 is one of the oldest open clusters with an age of ~8Gyr (Bedin, King, Anderson, Piotto, Salaris, Cassisi, and Serenelli, 2008), and also one of the most massive $\sim 4000 M_\odot$ (Kaluzny and Udalski, 1992; Kinman, 1965). Their size usually ranges between 3-10pc, such that they are much smaller than their distance from the Sun. Hence all the member stars are approximately at the same distance from the Sun. The stars in an open cluster are also of the same age and chemical composition. This is because they were all formed from the same giant molecular cloud.

1.3 COLOR-MAGNITUDE DIAGRAM (CMD)

A color magnitude diagram (CMD) is a scatter-graph of astronomical objects showing the relationship between each object's absolute magnitude and color. Alternatively, this graph can also be a relationship between luminosity and effective temperature. A CMD is a variant of the Hertzsprung-Russell Diagram (HRD), such that the HR diagram is a summary of temperature and magnitudes of all stars while a CMD is purposed to the study of star clusters.

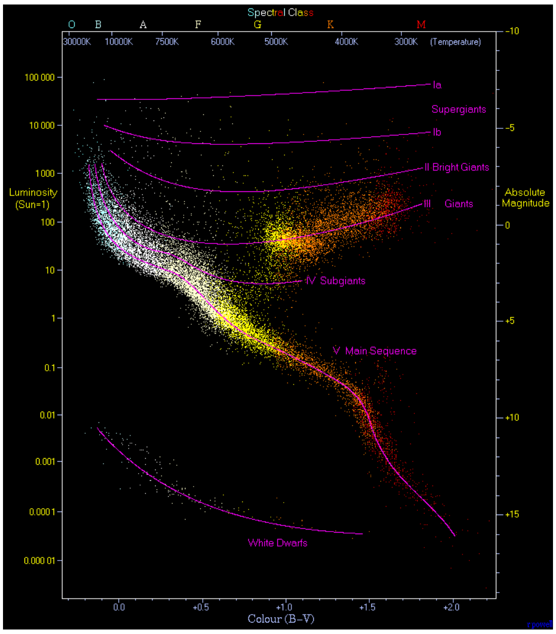

Figure 1.2: An observational Hertzsprung–Russell diagram with 22,000 stars plotted from the Hipparcos Catalogue and 1,000 from the Gliese Catalogue of nearby stars.

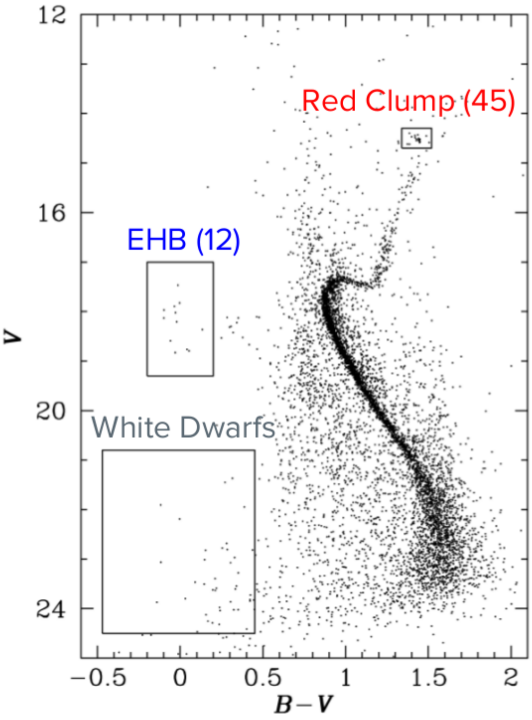

Figure 1.3: Color magnitude diagram of NGC 6791 in V vs B-V (Kalirai et al. (2007))

Figure 1.2 shows an HR Diagram that has 22,000 stars from the Hipparcos Catalogue and 100 from the Gliese Catalogue. The x-axis is the color (in this case B-V) or effective temperature. This axis represents the different spectral classes from hottest to coolest: O, B, A, F, G, K, and M. The y-axis is the luminosity or absolute magnitude (M_V in this case). This axis represents the luminosity classes from brightest to faintest: I (supergiants), II (bright giants), III (normal giants), IV (subgiants), V (main-sequence), sd (sub-dwarfs), and D (white dwarfs).

The CMD in figure 1.2 shows a grouping of many stars at about 5000K and $75L_\odot$. This region of the CMD is the Red Clump that have recently undergone a helium flash and are burning helium in their cores and hydrogen in a surrounding shell. The region adjacent to the red clump toward the colder (redder) end are the red giant stars which have a degenerate helium core with a hydrogen burning shell around.

1.4 Extended Horizontal Branch

Extended Horizontal Branch Stars are the result of a strong mass loss on the red giant branch (RGB). These stars have failed to reach the thermally pulsating stage on the asymptotic giant branch (AGB) after evolving off the zero-age horizontal branch (ZAHB). The extreme mass loss during the first ascent up the giant branch leaves only a very thin hydrogen envelope. The thin envelope exposes the hydrogen burning shell thus shifting the star toward the high temperature region of the H-R diagram. Hence these stars form a blue extension of the normal horizontal branch with $T_{eff} \approx 24,000 - 32,000$K. Such stars are usually found in low metallicity globular clusters like ω Cen (Whitney, O'Connell, Rood, Dorman, Landsman, Cheng, Bohlin, Hintzen, Roberts, Smith, Smith, and Stecher, 1994) and NGC 6752 (Buonanno, Caloi, Castellani, Corsi, Fusi Pecci, and Gratton, 1986; Castellani, degl'Innocenti, and Pulone, 1995) and in the case of higher metallicity populations, EHB stars are found in the metal rich open cluster NGC 6791 (Liebert, Saffer, and Green, 1994).

Some old quiescent elliptical galaxies show an enhancement in UV luminosity in their spectral energy distribution (SED). This "UV-upturn" in ellipticals and spiral bulges, seen short ward of 2000 Å, seems to characterize old stellar population in metal-rich environments (Bertola, Capaccioli, and Oke, 1982; Code and Welch, 1982). In these UV emissions, hot post-asymptotic giant branch (post-AGB) and extreme horizontal branch (EHB) stars are primary

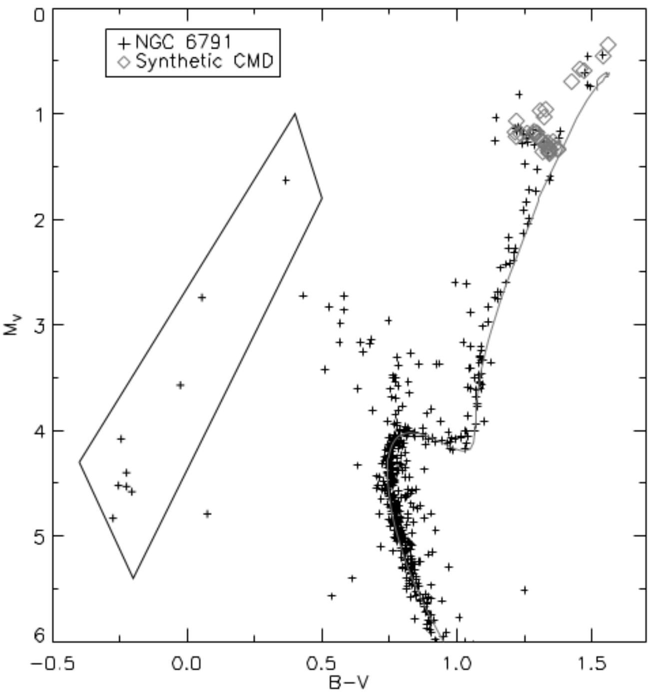

Figure 1.4: Observed Color magnitude diagram of NGC 6791 in V vs B-V (Yong et al. (2000)) along with a synthetic horizontal branch (in diamonds) Notice the absence of any EHB stars in the synthetic horizontal branch that has been prepared for a cluster age of 9Gyr.

contributors (Yi and Yoon, 2004). This "UV-upturn" from elliptical galaxies was one of the greatest mysteries of astrophysics for nearly 30 years in the 20th century. The "UV-upturn" is usually associated with the spectra of elliptical galaxies, but it was actually discovered in the bulge of the nearby spiral M31 (Code, 1969). By 1990, there were many candidates for the source of the UV emission, including hot white dwarfs, young massive stars, binaries, post-asymptotic giant branch (post-AGB) stars, extreme horizontal branch (EHB) stars, and non-thermal activity (Greggio and Renzini, 1990). Arguments based upon the fuel consumption during different evolutionary phases made EHB stars a likely source.

1.5 NGC 6791

NGC 6791 is an open cluster located in the Lyra constellation. It is located at (RA,DEC) (290.220°, +37.717°) and has an average radial velocity of -47.40 ± 0.20 kms^{-1} (Kamann, Bastian, Gieles, Balbinot, and Hénault-Brunet, 2019; Tofflemire et al., 2014). NGC 6791 is a relatively nearby cluster at a distance of about 4 kpc (Chaboyer, Green, and Liebert, 1999) from the sun. In the plane, it is located at 8 kpc from the galactic center, 1 kpc from the galactic plane, and at (l, b)=$(69.96^\circ, 10.90^\circ)$ (J2000). It is among the most massive ($\sim 4000 M_\odot$; Kaluzny and Udalski, 1992; Kinman, 1965) and populated, while also being one of the oldest (∼8Gyr; Bedin et al., 2008) open clusters. It has an unusually high metallicity ([Fe/H]$\sim 0.313 \pm 0.005$; Villanova et al., 2018 for its old age.

NGC 6791 remains a peculiar open cluster with a very old age and very high metallicity. It is an infamous outlier in all age-metallicity relations of Galactic disk objects. How did such a high metallicity object reach its current location 8kpc from the Galactic center and a kpc from the plane? (Geisler, Villanova, Carraro, Pilachowski, Cummings, Johnson, and Bresolin, 2012) suggested the presence of an intrinsic Na spread and even the slight Na-O anti-correlation, which led to the conclusion that NGC 6791 was the least massive star cluster hosting multiple stellar populations and the first open cluster to display the behavior. Villanova et al. (2018) gives concrete evidence for the origin of NGC 6791 in the Galactic bulge, with a non-negligible probability of originating from the Galactic Thin Disk. The Fig. 10 of Villanova et al. (2018) shows the position of NGC 6791 in the [Mg/Fe] vs [Fe/H] plane among the Galactic Bulge, Thin Disk, and Thick Disk. They find the cluster to be residing in the a region where only bulge stars are found. The question that remains unanswered is, how did it manage to move outwards atleast by 4 kpc during its lifetime. Several dynamical studies (Jílková, Carraro, Jungwiert, and Minchev, 2012; Martinez-Medina, Gieles, Pichardo, and Peimbert, 2018) find only a 0.1% probability that this actually happened, given all we know about the cluster and the Galactic potential and dynamics. However, this means we only need to have started with a few hundred to a thousand such clusters to find one today that actually achieved this feat. Also, in order to survive this radial migration over its lifetime, the original NGC 6791 must have been much more massive, about an order of magnitude. (Dalessandro, Miocchi, Carraro, Jílková, and Moitinho, 2015) uncovered evidence for tidal tails and mass loss from NGC 6791.

This open cluster, NGC 6791, exhibits a strong dual horizontal branch. In addition to the conventional red horizontal branch, it also harbors a very blue horizontal branch, the extended horizontal branch. It is vital to understand the origin and evolution of EHBs as it would have a significant impact on several areas of astronomy. For example, the study of globular cluster HB morphology constrains the formation history of the Milky Way Galaxy

(?)1978ApJ...225..357S). Also, as discussed in section 1.4, EHB stars contribute to the UV-upturn in elliptical galaxies. This open cluster could prove to be effective proxy to constrain the nature of the UV-upturn in elliptical and spiral bulges. It resembles an elliptical galaxy strongly owing to its peculiar hot/extended HB. Buzzoni, Bertone, Carraro, and Buson (2012) produce the spectral energy distribution (SED) of the NGC 6791 open cluster, and show that stars with $T_{eff} > 10,000$ K contribute to the UV luminosity shortward of 2500Å.

The global picture of HB morphology appears to be well understood. HB morphology is most affected by the metallicity of the cluster : more metal-rich clusters exhibit redder HBs ("first parameter" of HB morphology). However, observations in some globular clusters have shown HBs that have exhibited color distributions not expected for their metallicities. To explain this deviation, a "second parameter" is invoked: Age.

Figure 1.4 shows the CMD of NGC 6791 and it contains an observed CMD (Kaluzny and Rucinski, 1995) and a synthetic horizontal branch in diamonds (Yong et al., 2000). The EHB (hot HB) stars have been marked in a box. Note that the synthetic HB has only been able to reproduce the red clump, and does not contain any EHB stars, that is there are no diamonds away from the red clump. Even with an evolutionary age of 9 Gyr, this synthetic HB cannot reproduce anything close to the hot HB morphology of NGC 6791. Increasing the age by a couple of years produces some hot HB stars, but their number would still be smaller than observed. Therefore age effect seems to be insufficient in explaining the presence of EHB stars. Hence an alternate mechanism is in operation for the presence of these peculiar hot HB stars.

As discussed in in 1.4, EHB stars have undergone extreme mass loss during their first ascent up the RGB that they are left with a very thin envelope ($\sim 0.01 M_{\odot}$). We have ruled out two parameters: metallicity and age; of horizontal branch morphology to have any influence over the color bimodality in the horizontal branch. We try to find the cause for the presence of the extended horizontal branch, and in effect the cause for their loss of envelope. The loss of envelope can be attributed to two main causes: 1) Direct Mass loss, 2) Binary transfer.

1.5.1 DIRECT MASS LOSS

Every star undergoes mass loss while ascending up the red giant branch. The mass loss rate of our sun, though not in the RGB phase, is $10^{-14} M_{\odot} yr^{-1}$. One of the proposals to explain the stellar evolutionary path to the EHB stars in NGC 6791 is extreme mass loss owing to high metallicity of the cluster (D'Cruz, Dorman, Rood, and O'Connell, 1996; Kalirai et al., 2007; Yong et al., 2000). For EHB stars to form, mass loss rates of the order 10^{-9}–$10^{-10} M_{\odot}\mathrm{yr}^{-1}$ must be invoked as shown in Yong et al. (2000). On the other hand, Koopmann, Lee, Demarque, and Howard (1994) found an upper limit of $10^{-9} M_{\odot}\mathrm{yr}^{-1}$ for mass loss in horizontal branch stars evolving through the instability strip. Besides this limit, Michaud, Bergeron, Wesemael, and Fontaine (1985) set a stricter limit of $10^{-14} M_{\odot} yr^{-1}$, suggesting that a larger mass loss rate shall pose difficulty in reproducing the silicon underabundance in the sub-dwarf (sdB) branch stars. To invoke this kind of a mechanism, the mass loss must be "fine-tuned" for red giants to lose a lot of mass, but stop just short of losing the entire envelope. Furthermore, enhanced mass loss would accompany substantial circumstellar dust production. But, direct *Spitzer* observations do not reveal any such phenomenon (van Loon, Boyer, Dupree, Evans, Gehrz, McDonald, and Woodward, 2008). Thus, neither there is conclusive evidence for direct mass loss being the cause for formation of EHB stars, nor there is evidence for the occurrence of such mass loss.

1.5.2 BINARY TRANSFER

EHB stars that form the blue (hotter) end of the horizontal branch, have almost no envelope. On the other hand, red clump (RC) stars occupy the red end of the horizontal branch and possess an envelope after they have survived the helium flash at the RGB tip. The EHB and RC stars, have both evolved through the red giant branch (RGB) phase. At some point between the RGB phase and EHB phase, the envelope was lost almost completely. This could be due to loss of matter to a binary companion. If binary transfer is the cause for a lack of envelope in the EHB stars, we expect to find binary stars in the RGB phase as well. Binary stars in the RGB phase will evolve to form the EHB, while non-binaries will form the RC. Hence, the ratio of the number of binary stars to non-binary stars in the RGB must agree to the ratio of the number of stars in the EHB to RC.

$$\frac{\text{Binaries in RGB}}{\text{Non-binaries in RGB}} = \frac{\text{EHB}}{\text{RC}}. \tag{1.2}$$

Binary evolution provide a natural mechanism of depleting the hydrogen-rich outer layer of the star without invoking ad-hoc or simplified mass loss methods. Carraro and Benvenuto (2017) employ an updated form of the Benvenuto and De Vito (2003) binary evolution code to demonstrate that EHBs can emerge from the post-CE (common envelope) evolution (Carraro, Girardi, Bressan, and Chiosi, 1996; Liebert et al., 1994) of binary stars with masses conducive to the cluster's turn-off ($M = 1.5 M_\odot$). They find that mass transfer to the companion is unstable and thus a common envelope (CE) engulfs the stars. Apart from binary transfer, mass loss can also lead an isolated star to reach the EHB, but a binary track is preferred since it does not require ad-hoc anomalies and unconfirmed mass loss rates. No other open cluster is known to harbor an EHB star, implying that they may be less massive than NGC 6791, even though they host a comparable amount of binary stars. EHB stars are more common in globular clusters, but they are located centrally in globular clusters (GCs) unlike NGC 6791. In GCs, they also span a wider range of colors (temperature). This was historically interpreted with the existence of a wide range of envelope sizes, hence with differential mass loss during the RGB ascent. The segmented EHB is mostly interpreted as evidence of multiple stellar generations, each segement with a different degree of He enhancement. Evidence for multiple stellar population is lacking for NGC 6791.

NGC 6791 exhibits a binary percentage of 50% (Bedin et al., 2008; Twarog, Carraro, and Anthony-Twarog, 2011), and three have been three confirmed binary systems in the EHB population: B4 (Mochejska, Stanek, and Kaluzny, 2003; Pablo, Kawaler, and Green, 2011), B7, and B8 (Mochejska et al., 2003; van den Berg, Verbunt, Tagliaferri, Belloni, Bedin, and Platais, 2013). Hence, it is probable that the RGB stars that were in binary systems during the RGB ascent, lost their envelopes and made the extreme horizontal branch. Whereas the RGB stars that were not in binary systems formed the red clump (RC). There are approximately 45 stars occupying the RC (Buzzoni et al., 2012) and about 12 EHB stars. Recalling equation 1.2,

$$\frac{\text{Binaries in RGB}}{\text{Non-binaries in RGB}} = \frac{\text{EHB}}{\text{RC}} = \frac{12}{45} = \frac{4}{15} = 0.267. \tag{1.3}$$

We thus expect to find the ratio of binary to non-binary stars to be 0.267 in the sample of our RGB stars, that is a binary percentage of $0.267/(1 + 0.267) = 0.211$ in the total sample of RGB stars. For our sample of 16 RGB stars, we expect to find $0.211 \times 16 = 3.3$ $(3 - 4)$ binaries, to be able to consider binarity to be a plausible cause for the formation of EHB stars.

1.6 OVERVIEW

The analysis in this master thesis was done with photometric data from previous studies (Brogaard, Vandenberg, Bruntt, Grundahl, Frandsen, Bedin, Milone, Dotter, Feiden, Stetson, Sandquist, Miglio, Stello, and Jessen-Hansen, 2012; Stetson, Bruntt, and Grundahl, 2003) and the spectra taken with the FLAMES [*] GIRAFFE spectrograph at ESO [†] VLT [‡]. We have multi-epoch spectra of 16 red giants in the open cluster NGC 6791 and we will aim at finding binaries among these to support our hypothesis: binarity as the cause for the presence of extreme horizontal branch stars in NGC 6791.

The structure of the thesis will be taken forward as follows. In chapter 2 we will discuss about the spectral data used and the identification of objects, and the reduction procedure for all the spectra. In chapter 3, we will calculate stellar parameters (effective temperature, surface gravity, and microturbulence) from photometry. After the successful calculation of these parameters, in chapter 4 we will see how these properties can be used to prepare model atmospheres, prepare synthetic spectra, and calculate radial velocities of stars. Finally, in the conclusion we will discuss about the radial velocity curves obtained for our stars. We shall further check if we indeed succeed in finding any binary stars and how strongly does this support our assertion of a direct between EHB formation in NGC 6791 and binarity.

---

[*] Fibre Large Array Multi Element Spectrograph

[†] European Southern Observatory

[‡] Very Large Telescope

NI have noticed even people who claim everything is predestined, and that we can do nothing to change it, look before they cross the road.

Stephen Hawking

2

Data

The spectroscopic data used here was observed using FLAMES GIRAFFE spectrograph. GIRAFFE is a medium-high resolution (R=5500–65000) spectrograph for the entire visible range 3700–9000Å. Interestingly, the name comes from the first design where the spectrograph was standing vertically on a platform.

2.1 Observations

Observations were carried out for 16 RGB stars in the open cluster NGC 6791. We have multi-epoch spectra for each star which will help us find binary systems in our sample of 16 stars. For each star we have spectra from at least 4 different epochs and at most 8. The total number of observations of each star is shown in table 2.1. The exposure time for each observation was 2640 seconds (44 minutes). Assuming that the period of binary stars we expect to find is of the order of a few days, this exposure time length would be of little significance. The wavelength range of our observations is from $6114.0 - 6404.0$Å. The signal-to-noise ratio (SNR) of the spectra ranges from 19.5 to 105.1.

Table 2.1: Object IDs and their individual number of observations

OBJECT ID	KIC ID	2MASS ID	GAIA DR2 ID	No. of observations
RGB.14789	2436849	J19204429+3746129	2051293152424244992	8
RGB.15000	2436884	J19204485+3746215	2051293152424246912	8
RGB.16554	2437103	J19204873+3747124	2051293186784001152	8
RGB.17278	2437222	J19205058+3747336	2051293289863224832	4
RGB.17636	2437270	J19205143+3746408	2051292976340888448	4
RGB.17671	2437281	J19205151+3745461	2051292980625563520	8
RGB.17778	2437296	J19205180+3746481	2051293083704790016	4
RGB.18045	2437325	J19205243+3747152	2051293289863225728	8
RGB.18071	2437327	J19205245+3746045	2051292980625569280	8
RGB.18535	2437402	J19205358+3747188	2051293083704797952	8
RGB.19104	2437488	J19205499+3745410	2051292911906095360	4
RGB.20213	2437653	J19205784+3747067	2051293118064542976	4
RGB.21185	2437781	J19210043+3747160	2051293427302192640	8
RGB.21350	2437804	J19210086+3745339	2051105342096702080	4
RHB.15187	2436912	J19204532+3747179	2051293255503469184	5
RHB.21348	2437805	J19210086+3746396	2051293049345067904	7
				TOTAL: 100

2.2 Object Identification

We have at our disposal a total of 100 spectra from 16 RGB stars of NGC 6791. It is of crucial importance to identify these 16 stars. This identification was possible using the right ascension (RA) and declination (DEC) given in the headers of the observation FITS (Flexible Image Transport System) files. These RA and DEC values were used as inputs into the SIMBAD [*] database to identify objects in the closest vicinity of the input coordinates. A radius of 2 arc-seconds was defined to identify target objects. In order to be sure of these results, a manual check was carried out with Aladin Lite [†].

The 16 objects were thus identified in the GAIA data base, KIC catalogue, and 2MASS survey. The respective IDs of these stars are given in table 2.1.

---

[*] http://simbad.u-strasbg.fr/simbad/sim-fid

[†] https://aladin.u-strasbg.fr/AladinLite/

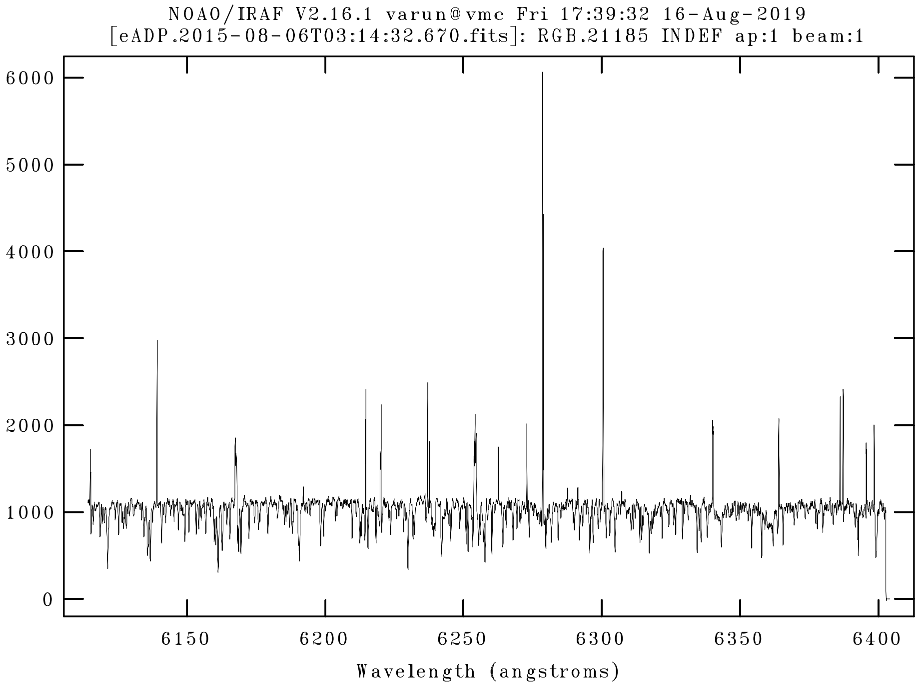

Figure 2.1: Image of a spectra of RGB.21185. Notice the strong emission lines that almost reach $>$6000 in relative flux units. Except the emission line at 6300.3Å, all are a result of cosmic rays. The 6300.3Å emission line is due to the atmospheric OI.

2.3 REDUCTION PROCEDURE

The spectra at hand had been partially reduced through the ESO pipeline [‡]. Hence, the spectra now needs to be only reduced for the following:

1. Cosmic Rays: Cosmic rays are ultra-high energy particles that fall on earth. When they interact with our atmosphere, the particles break up into even smaller particles: electrons, photons, and muons. Our GIRAFFE detector has also caught some of these particles, that has resulted in the presence of arbitrary emission lines in the spectra as seen in figure 2.1. These cosmic ray features were removed using the task `LINECLEAN` in IRAF[§]. The *spline*1 (a linear spline) function was used. The initial parameters were

---

[‡] https://www.eso.org/sci/software/pipelines/giraffe/giraffe-pipe-recipes.html

[§] The Image Reduction and Analysis Facility, a general purpose software package for astronomical data, is written and supported by the IRAF programming group of the National Optical Astronomy Observatory (NOAO) in Tucson, AZ, USA. http://ast.noao.edu/data/software

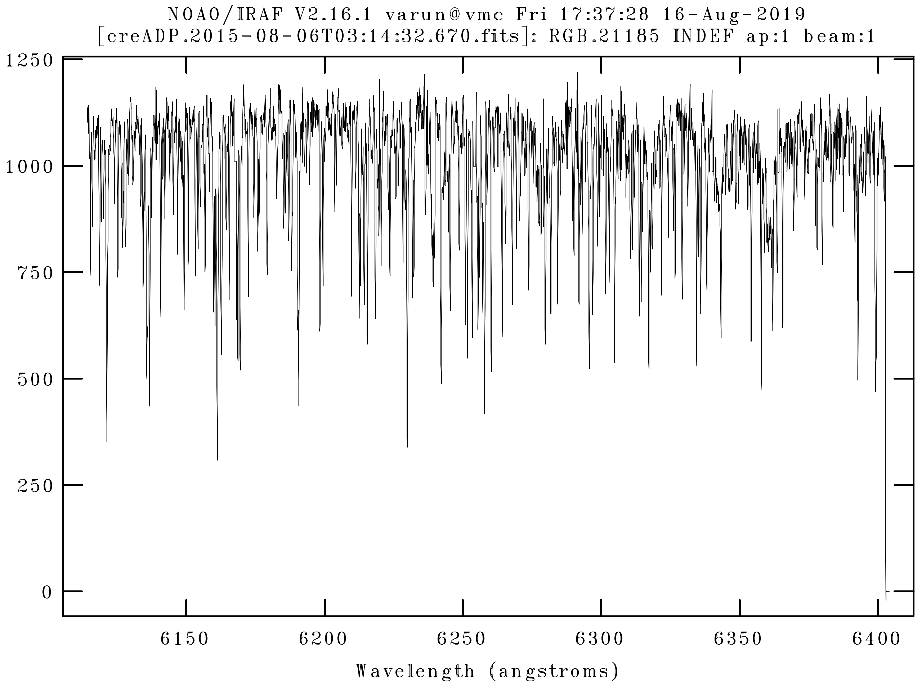

Figure 2.2: Image of a cleaned spectra of RGB.21185

set as follows: *order=1, low_rejection=0, high_rejection=1.2, niterate=1, grow=0*. All spectra were cleaned individually and hence parameters were adjusted accordingly.

2. OI 6300.3Å Atmospheric Emission Line: This emission line was also cleaned using the `LINECLEAN` task along with the cosmic ray emission lines. A cleaned spectra, with most of the emission line features is shown in figure 2.2.

3. Continuum Normalization: The cleaned spectra is yet not completely available for analysis. The unit for the strength of the lines (y-axis) of the spectra is in arbitrary flux units and there is need for normalization. Hence, we find suitable functions to fit the continuum flux, and normalize the spectra using this continuum function as the reference (reference set to 1). For this purpose, we use the task `CONTINUUM` in IRAF. We employe a spline function of degree 3 (*spline*3) to fit continuum of individual spectra. The initial parameters were set as follows: *type=ratio, order=5, low_rejection=0.8, high_rejection=4, niterate=10*. After continuum normalization, the final spectra obtained is shown in figure 2.3

4. Wavelength Shift: The spectra is in the heliocentric frame of reference, i.e. the doppler shift in the spectra corresponds to the velocity of the star with respect to the sun. Hence, to bring the spectra to rest (laboratory) wavelength we need to find the shift

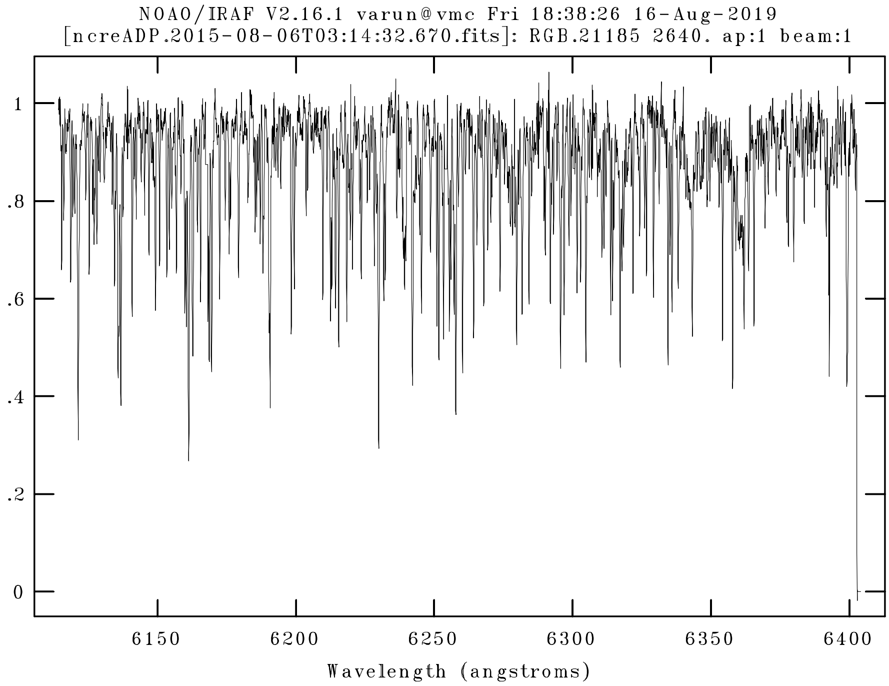

Figure 2.3: Image of a cleaned spectra of RGB.21185

in wavelength. For this shift to be determined, we use the task FXCOR[¶] to find the radial velocities from individual spectra. The radial velocities will be calculated in section 4.3. These radial velocities will then be translated into a wavelength shift using the `DOPCOR`[‖].

We finally have a spectra that is ready to be used for analysis. The spectra has been cleaned for cosmic ray showers and atmospheric emission lines, and has been continuum normalized. The spectra is ready to be used for making radial velocity measurements and consequently abundance analysis (after wavelength correction). But for the purpose of radial velocity measurements using `FXCOR`, we first need to prepare a synthetic spectra. The preparation recipe for this is discussed in chapter 3.

[¶] Fourier Cross Correlation

[‖] Doppler Correction

My eyes are constantly wide open to the extraordinary fact of existence. Not just human existence, but the existence of life and how this breathtakingly powerful process, which is natural selection, has managed to take the very simple facts of physics and chemistry and build them up to redwood trees and humans.

Richard Dawkins

3

Stellar parameters and Photometry

A STAR IN LOCAL THERMODYNAMIC EQUILIBRIUM (LTE) can be quantified using four parameters:

1. Effective Temperature (T$_{eff}$): Every object emits and absorbs radiations (photons). A black body in thermal equilibrium emits electromagnetic radiation according to the Planck's law. The effective temperature of star is the effective temperature of a black body if it were to emit the same amount of surface flux as the star. In other terms, the temperature for which Planck's law gives the total spectral irradiance area same as that for the observed star, is the effective temperature of the star.

2. Metallicity ([Fe/H]): The metallicity [Fe/H] of a star is defined with respect to the iron abundance of sun.

$$[Fe/H] = \log_{10}\left(\frac{Fe}{H}\right)_{\star} - \log_{10}\left(\frac{Fe}{H}\right)_{\odot} \tag{3.1}$$

$\left(\frac{Fe}{H}\right)$ is the number ratio of the Fe and H atoms, where $\star$ represents the value for the star and $\odot$ is solar value.

3. Surface Gravity (g): Surface gravity of a star is the gravitational acceleration experienced at the surface on the equator. The surface gravity of earth, $g_{earth} = 9.8\mathrm{ms}^{-2}$ and that of the sun is $28.02 g_{earth}$.
4. Micro-turbulence (ξ): As the term itself suggests, microturbulence is the turbulence over small distance scales. These small scale motions in the stellar atmosphere cause additional broadening of stellar spectra. This broadening is in addition to the already existing thermal broadening.

Every star will possess a unique combination of these stellar parameters. These can be determined either from spectroscopy or photometry. The range of our spectra is only about 290Å(6114–6404Å). For the determination of stellar parameters using spectroscopy, we need to make use of absorption lines. For an accurate determination, it is important to have many such lines (atleast 50) in our spectral range. But in a span of 290Å, not many significant atomic absorption lines are present. It is thus best to determine the stellar parameters using photometry.

3.1 EFFECTIVE TEMPERATURE

The effective temperature is related to the color of a star. In order to have consistency in all our measurements, it should be made sure that photometric data is available for all stars from a single study. B band and V band magnitudes were available in full from the photometric studies of NGC 6791 in Stetson et al. (2003) and Brogaard et al. (2012). The effective temperatures calculated from these studies are then averaged as shown in table 3.2.

We use the color-T$_{eff}$ relation given in Alonso, Arribas, and Martínez-Roger (1999) to find the effective temperature from the B-V color. The colors are corrected for extinction E(B-V)=0.12 (An, Pinsonneault, Terndrup, and Chung, 2019),

$$(B-V)_{observed} - (B-V)_{corrected} = E(B-V)$$

The relation color-T-$_{eff}$ relation is then given as follows,

$$\theta_{\text{eff}} = a_0 + a_1 X + a_2 X^2 - a_3 X[\text{Fe/H}] + a_4[\text{Fe/H}] + a_5[\text{Fe/H}]^2 \tag{3.2}$$

Table 3.1: Coefficient (a_i) values based on color ranges.

Color range	a_0	a_1	a_2	a_3	a_4	a_5
0.20 < (B-V) < 0.80	0.5716	0.5404	-6.126e-2	-4.862e-2	-1.777e-2	-7.969e-3
0.70< (B-V) < 1.90	0.6177	0.4354	-4.025e-3	5.204e-2	-0.1127	-1.385e-2

Table 3.2: The B-V colors, V band magnitude, and B band magnitude of our stars along with their calculated effective temperatures.

Object ID	V_{St}	B_{St} - V_{St}	$T_{eff,St}$	V_{Br}	B_{Br}-V_{Br}	$T_{eff,Br}$	$T_{eff,avg}$
RGB.14789	16.28	1.32	4507.32	16.27	1.32	4503.75	4505.53
RGB.15000	14.14	1.57	4107.20	14.12	1.57	4108.67	4107.94
RGB.16554	14.82	1.41	4364.23	14.82	1.40	4374.27	4369.25
RGB.17278	16.34	1.20	4745.84	16.34	1.18	4765.73	4755.79
RGB.17636	15.31	1.33	4486.04	15.30	1.33	4501.98	4494.01
RGB.17671	15.99	1.22	4700.75	15.99	1.21	4714.38	4707.57
RGB.17778	16.40	1.24	4654.62	16.40	1.23	4671.81	4663.21
RGB.18045	15.70	1.31	4528.80	15.70	1.30	4541.43	4535.12
RGB.18071	15.28	1.35	4459.73	15.27	1.34	4471.97	4465.85
RGB.18535	15.12	1.39	4389.40	15.11	1.39	4396.16	4392.78
RGB.19104	15.38	1.36	4445.83	15.38	1.35	4461.47	4453.65
RGB.20213	15.52	1.35	4464.96	15.52	1.34	4480.75	4472.86
RGB.21185	15.65	1.34	4468.46	15.64	1.33	4484.27	4476.37
RGB.21350	14.55	1.41	4357.57	14.54	1.40	4370.92	4364.25
RHB.15187	14.60	1.36	4438.91	14.60	1.36	4447.56	4443.23
RHB.21348	14.58	1.37	4419.99	14.57	1.36	4433.73	4426.86

where $\theta_{\text{eff}} = \frac{5040}{T_{\text{eff}}}$, X is the color, [Fe/H] is the metallcity, and a_i‘s are the coefficients of the polynomial. The values of a_i‘s are given in table 3.1 according to the range of B-V color. The cluster metallicity for NGC 6791 has been estimated at 0.31 ± 0.005 by Villanova et al. (2018). We hence assume this metallicity as constant throughout all the stars under study.

3.2 SURFACE GRAVITY

After having estimated the effective temperatures of our stars, we now need to estimate the surface gravity. For this purpose, we make use of PARSEC[*] evolutionary tracks. The isochrones

---

[*] The stellar evolutionary code to generate ischrones can be found at `http://stev.oapd.inaf.it/cgi-bin/cmd` (Bressan, Marigo, Girardi, Salasnich, Dal Cero, Rubele, and Nanni, 2012)

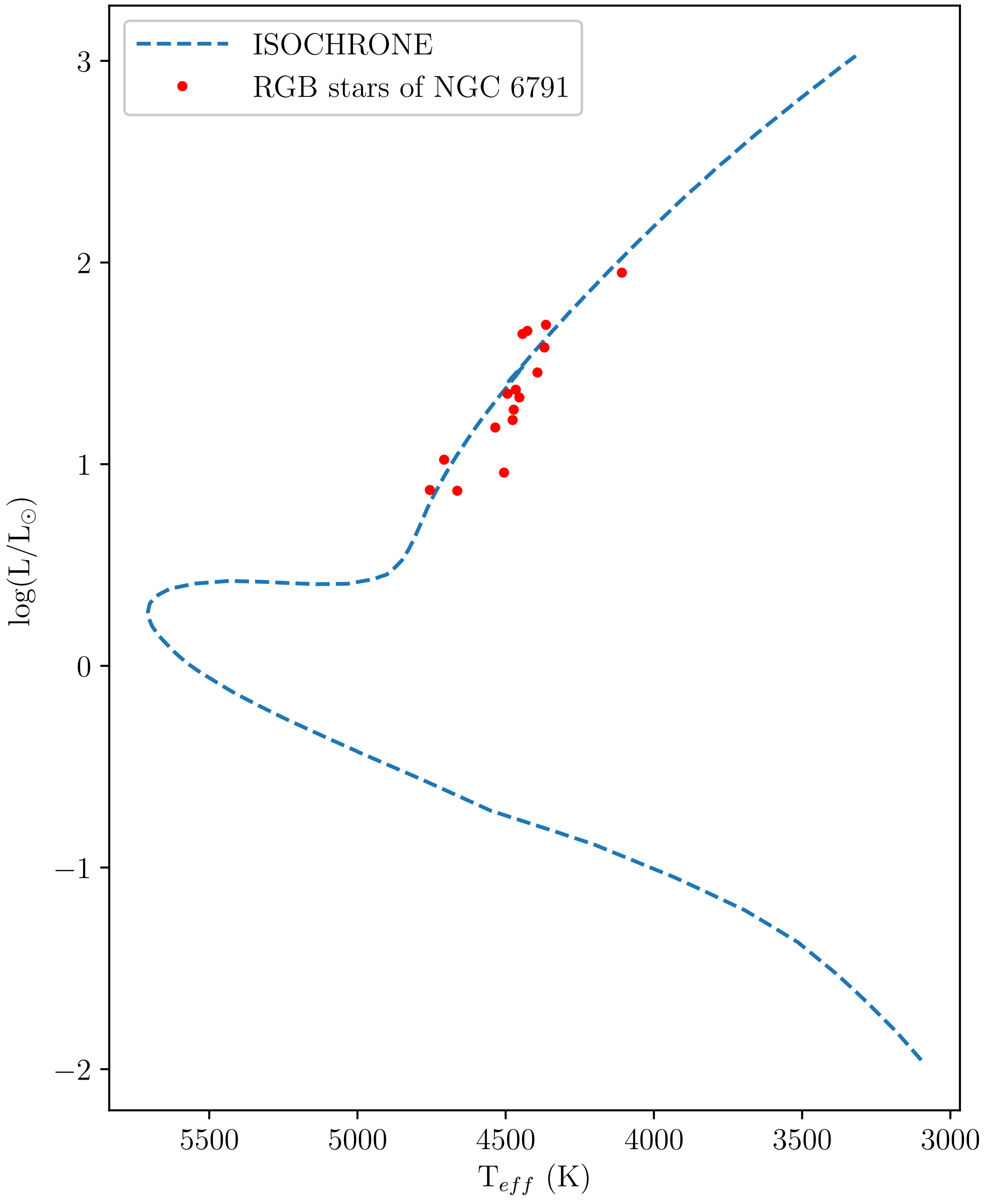

Figure 3.1: The blue dashed line shows the isochrone for NGC 6791 with an age of 8Gyr and metal fraction (Z) of 0.04. The red dots are the respective stars under study.

are modeled with an age of 8 Gyr for NGC 6791 (Bedin et al., 2008) and with an initial metal fraction Z$_{ini}$ is 0.04.

The surface gravity can thus be calculate using the realation:

$$\log(g) = \log(g_\odot) + \log\left(\frac{M}{M_\odot}\right) + 4 \cdot \log\left(\frac{T_{eff}}{T_{eff,\odot}}\right) - \log\left(\frac{L}{L_\odot}\right) \tag{3.3}$$

and

$$\log\left(\frac{L}{L_\odot}\right) = -0.4(M_V + BC_V - M_{BC,\odot}) \tag{3.4}$$

,

where g is the surface gravity of our stars, M is the mass, T_{eff} is the effective temperature,M_V is the absolutely magnitude in V band, BC_V is the bolometric correction in V band and L is luminosity. The $\odot$ symbol represents solar values where $T_{eff,\odot} = 5777K$, $\log(g_\odot) = 4.44$ dex, $M_{BC,\odot} = 4.74$. The mass of these stars are extracted from the isochrone. The absolute magnitude M_V can be calculated from the apparent magniude (m_V or V) using the distance modulus,

$$m_V - M_V = 5\log(d) - 5 \tag{3.5}$$

where d is the distance to the cluster from the sun in parsecs (pc). The distance modulus for NGC 6791 is 13.43 (WEBDA †). The bolometric correction (BC_V) is derived for each star using the relation in Alonso et al. (1999).

$$\begin{split} BC_V = \frac{-5.531 \cdot 10^{-2}}{X} - 0.6177 + 4.420X - 2.669X^2 + 0.6943X \\ \cdot [Fe/H] - 0.1071[Fe/H] - 8.612 \cdot 10^{-3}[Fe/H]^2 \end{split} \tag{3.6}$$

As you can see in figure 3.1, the blue dashed lines represent the isochrone of the open cluster

---

† https://webda.physics.muni.cz/cgi-bin/ocl_page.cgi?cluster=Ngc+6791

Table 3.3: A complete table of stellar properties of all the 16 stars under study. The metallicity of the stars is taken as the cluster metallicity which is 0.313±0.005 (Villanova et al., 2018)

Object ID	Mass ($M_\odot$)	T_{eff}	$\log L/L_\odot$	$\log(g)^{\ddagger}$	Microturbulence (ξ)
RGB.14789	1.15	4505.53	0.96	3.11	0.56
RGB.15000	1.15	4107.94	1.95	1.96	1.13
RGB.16554	1.15	4369.25	1.58	2.44	1.01
RGB.17278	1.14	4755.79	0.87	3.29	0.70
RGB.17636	1.15	4494.01	1.35	2.71	0.90
RGB.17671	1.14	4707.57	1.02	3.12	0.79
RGB.17778	1.15	4663.21	0.87	3.26	0.61
RGB.18045	1.15	4535.12	1.18	2.90	0.79
RGB.18071	1.15	4465.85	1.37	2.68	0.90
RGB.18535	1.15	4392.78	1.45	2.57	0.91
RGB.19104	1.15	4453.65	1.33	2.72	0.85
RGB.20213	1.15	4472.86	1.27	2.79	0.82
RGB.21185	1.15	4476.37	1.22	2.84	0.77
RGB.21350	1.15	4364.25	1.69	2.32	1.10
RHB.15187	1.15	4443.23	1.65	2.40	1.13
RHB.21348	1.15	4426.86	1.66	2.38	1.13

whereas the red dots are the stars under study. The RGB stars are plotted along the isochrone using effective temperature and luminosity from table 3.2 and they can be seen lying on the red giant branch.

3.3 MICRO-TURBULENCE

Once the effective temperature and surface gravities of all the stars are calculated, we have everything we need to calculate the microturbulence velocity. Using the relation given in Gratton, Carretta, and Castelli (1996),

$$\xi = 1.19 \cdot 10^{-3} T_{eff} - 0.90 \log(g) - 2 \tag{3.7}$$

where ξ is the microturbulence velocity in kms^{-1} and g is the surface gravity in cgs units of cms^{-2}. The measured surface gravities are given in table 3.3.

We have now measured the effective temperature, surface gravity, and microturbulence velocity for all our target stars. All the physical properties are enlisted in table 3.3. The metallicity has been set to be 0.313 for all stars. These parameters are now enough for the preparation recipe of synthetic spectra of our stars.

What can be asserted without evidence can also be dismissed without evidence.

Christopher Hitchens

4

Radial Velocities

THE CALCULATION OF RADIAL VELOCITIES involves comparing our observed spectra (in the heliocentric frame of reference) to a synthetic spectra (in the laboratory/rest/star frame of reference). The wavelength shift between these two spectra gives the Doppler shift (z).

$$z = \frac{\lambda_{obs} - \lambda_{rest}}{\lambda_{rest}} \tag{4.1}$$

$$v = z/c \tag{4.2}$$

where λ_{obs} is the wavelength in the observed spectra, λ_{rest} is the wavelength in the rest (synthetic) spectra, c is the speed of light, and v is the velocity of the star with respect to the frame of reference of the observed spectra. One way to measure redshift and velocity is to use individual absorption lines. The wavelength of specific lines are identified in both the spectra and is then used in equation 4.1. For a very accurate determination, if done manually for each line, this method will involve using hundreds of lines to make Doppler shift calculations. This process for hundred spectra would be time-inefficient and also lack accuracy. Hence, we

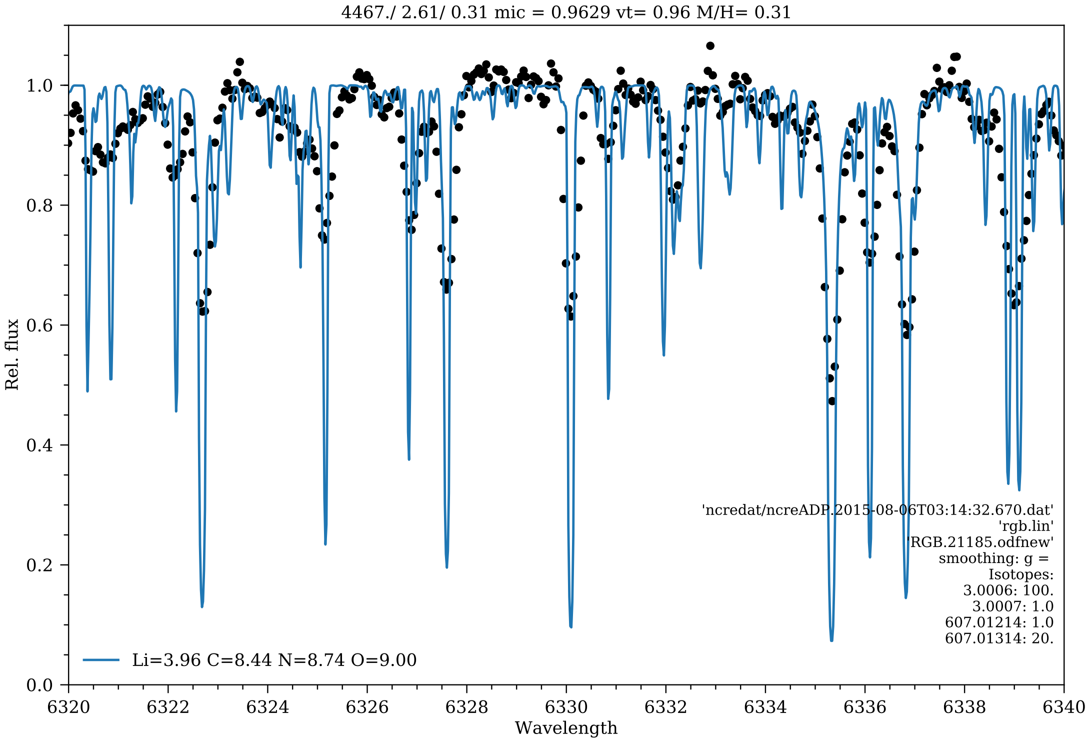

Figure 4.1: A synthetic spectra (in blue) of RGB.21185 along with the original observed spectra. The synthetic spectra is smoothed with a gaussian factor of 0.0. The observed spectra has been shifted by 43.76 kms^{-1} for better comparison with the synthetic spectra.

employ the method of cross-correlation between the observed spectra and synthetic spectra to find the velocity.

4.1 SYNTHETIC SPECTRA

Preparation of synthetic spectra requires four important stellar parameters namely: effective temperature, surface gravity, metallicity, and microturbulence. These parameters are used to prepare stellar model atmospheres that contain information about the distribution of main physical quantities (temperature, pressure) with geometrical depth. Stellar atmosphere models required by the analysis are from the Castelli, Gratton, and Kurucz (1997) and Castelli and Kurucz (2003) grid [*] of model atmospheres.

---

[*] Available at `http://kurucz.harvard.edu/grids.html`

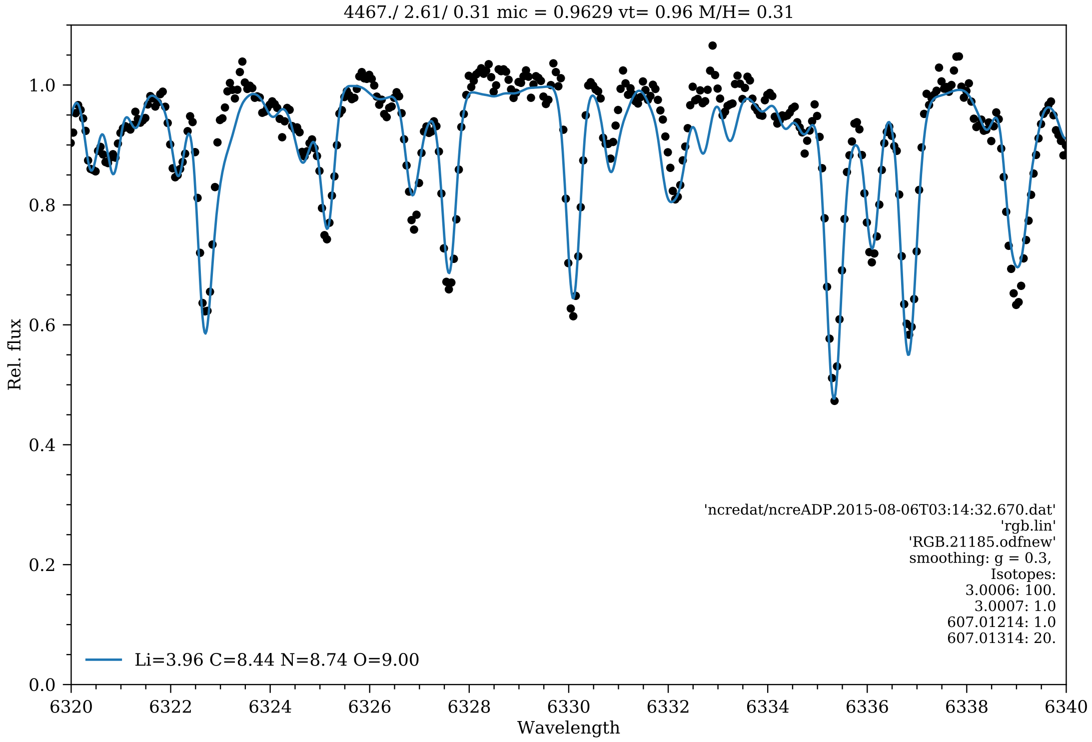

Figure 4.2: A synthetic spectra (in blue) of RGB.21185 along with the original observed spectra. The synthetic spectra is smoothed with a gaussian factor of 0.3. The observed spectra has been shifted by 43.76 kms^{-1} for better comparison with the synthetic spectra.

To prepare the synthetic spectra, apart from the model atmosphere that gives information about the physical properties of the stellar photosphere, a linelist is required that gives information about the properties of absorption lines. A linelist contains the following information about the absorption line: wavelength (λ), atomic number (Z) and degree of ionization (n) (Z.N eg. 26.0 for neutral Iron, 22.1 for singly ionized Titanium etc.), transition probabilities ($\log(gf)$, and excitation potential (E.P.). We obtain our linelist using the LINEMAKE code [†] that produces MOOG-compatible synthesis line list by starting with the Kurucz compendium [‡] and then substituting, adding, splitting, etc., these lists to employ the excellent atomic data from the Wisconsin group (Jim Lawler and associates) and excellent molecular data from the Old Dominion group (Peter Bernath and associates). Line list is prepared for the range $6114 - 6405$Å to contain the wavelength range for our spectra.

After we have the model atmospheres for all the stars using the KURUCZ grid models and linelist with the LINEMAKE code we can now prepare the synthetic spectra. We used the LTE (local thermodynamic equilibrium) line analysis and spectrum synthesis code MOOG[§] (Sneden, 1973), implemented in the Python wrapper pyMOOGi[¶], to prepare the synthetic spectra. The wavelength step is set at 0.02Å and the gaussian smoothing factor is set to be 0.3. The small (yet finite) wavelength step ensures that there are enough data points to correlate with the observed spectra. Where as, the smoothing factor makes the spectra have a finite resolution. A zero gaussian smoothing factor will produce a spectra with no noise, and hence infinite resolution as shown in figure 4.1. Thus, it is important to introduce noise into the synthetic spectra manually with the help of a smoothing factor as can be seen in figure 4.2.

4.2 FOURIER CROSS CORRELATION (`FXCOR`)

The synthetic spectra for the 16 RGB stars have now been prepared. In order to find the Doppler shift we use a fourier cross correlation task `FXCOR` provided by IRAF. Cross correlation is the measure of similarity between two signals as a function of displacement of one relative to the other. `FXCOR` takes as input the object (observed) spectra and the template (synthetic spectra). It then plots the correlation strength (similarity) versus the velocity shift

---

[†] Available at `https://github.com/vmplacco/linemake`

[‡] `http://kurucz.harvard.edu/linelists.html`

[§] Available at `https://www.as.utexas.edu/~chris/moog.html`

[¶] Available at `https://github.com/madamow/pymoogi`

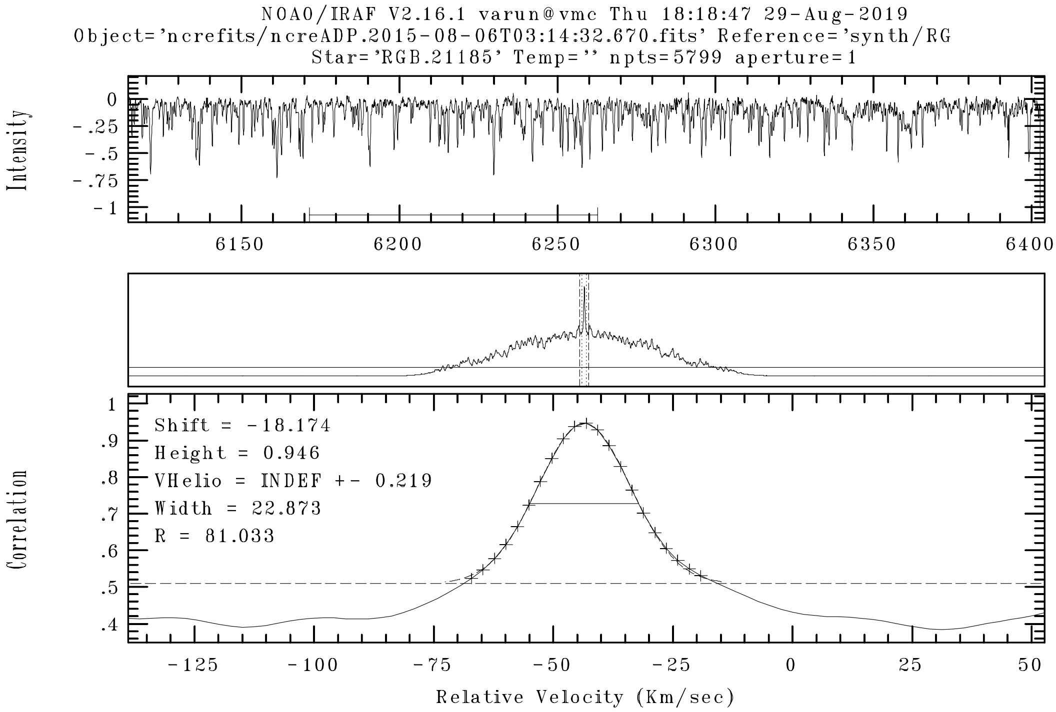

Figure 4.3: The fourier cross correlation function in use for one of the spectra of RGB.21185. The velocity calculated for this is -43.76 ± 0.20kms^{-1}.

(displacement) as shown in the bottom panel of figure 4.3.

The correlation function can change depending on the region of the spectra that is chosen for correlation. We must avoid using the region around 6300±200Å for the cross-correlation as this region is highly influenced by telluric absorptions. For every spectra, an attempt is made to maximize the R parameter, also known as the Tony & Davies R (TDR) parameter. The TDR parameter is a proxy for the goodness of the cross-correlation. Smaller TDR represents larger uncertainties in velocity and therefore to a poor fit. Take a look at one of the correlation functions in figure 4.3. The correlation peak is manually fitted with a Gaussian function. This peak value corresponds to the displacement at which there is maximum similarity, which in this case is at -43.76 ± 0.20 kms^{-1} for RGB.21185.

4.3 RADIAL VELOCITIES

The `FXCOR` task is used with the 100 spectra. Radial velocities for the 16 RGB stars are given in tables 4.1 – 4.16. A correlation height of greater than 0.88 and TDR parameter greater than 50 is achieved across all radial velocity measurements. Figure 4.4 shows the radial velocity curve for all the objects in individual panels with object name in the title. The red points are the radial velocities along with error bars, the red dashed line is the average radial velocity for that object, and the shaded red region is the standard deviation in the radial velocities of the object. The green continuous line is the cluster velocity which is 47.40±0.20kms^{-1} (Kamann et al., 2019; Tofflemire et al., 2014) and the shaded green region is the error in the cluster velocity (this error has been taken as the average of error in measurement of radial velocities of our objects). It can be seen that variation in radial velocities is observed in some of the objects, which could be an indication of a binary system.

Figure 4.5 also shows the radial velocities for all objects on a single plot. The blue dashed line is the cluster velocity and the shaded region is the error in cluster velocity. In table 4.17, all the velocities are listed along with average radial velocity of the object (V$_{avg}$) average of error in all radial velocities (V$_{err,\text{avg}}$), standard deviation in the radial velocities (σ_V), and the ratio of the standard deviation to the average RV errors (let's call this the the Binary factor (Bf)).

Apart from the multi-epoch radial velocity measurements in our study, there is a similar

Table 4.1: Radial velocity measurements using FXCOR for object **RGB.14789** along with errors, correlation strength, and the Tony & Davies R (TDR) parameter.

HJD-245000	Velocity (kms^{-1})	V_{err} (kms^{-1})	Corr. Height	TDR
7195.71290	-28.65	0.26	0.92	68.09
7195.75285	-29.05	0.26	0.92	67.93
7197.74783	-28.25	0.23	0.92	73.13
7200.68977	-28.32	0.27	0.91	63.66
7200.72891	-28.45	0.29	0.9	59.75
7200.77191	-28.29	0.27	0.88	63.64
7214.66612	-28.82	0.32	0.89	54.32
7214.70742	-28.84	0.25	0.91	69.12

Table 4.2: Radial velocity measurements using FXCOR for object **RGB.15000** along with errors, correlation strength, and the Tony & Davies R (TDR) parameter.

HJD-245000	Velocity (kms^{-1})	V_{err} (kms^{-1})	Corr. Height	TDR
7195.71289	-44.71	0.17	0.95	103.46
7195.75285	-44.93	0.18	0.95	94.53
7197.74783	-44.42	0.19	0.95	96.35
7200.68977	-44.79	0.17	0.95	104.84
7200.72890	-44.89	0.24	0.94	72.66
7200.77191	-44.71	0.18	0.95	99.42
7214.66612	-45.29	0.21	0.95	83.83
7214.70742	-45.33	0.18	0.95	94.69

study of NGC 6791 stars in Tofflemire et al. (2014) from the WIYN open cluster study. The radial velocity data base of this study was cross searched for stars in our study and matches were found for the following 13 stars: RGB.15000, RGB.16554, RGB.17636, RGB.17671, RGB.18045, RGB.18071, RGB.18535, RGB.19104, RGB.20213, RGB.21185, RGB.21350, RHB.15187, and RHB.21348. The radial velocities from the WIYN study are overplotted on figure 4.4, and the final combined radial velocity curve is shown in figure 4.6. Unfortunately, the WIYN study measurements did not deliver errors in the RVs in their data base. Hence these data points will be used solely for the purpose of complimenting our RVs without using them to draw conclusions.

Table 4.3: Radial velocity measurements using FXCOR for object **RGB.16554** along with errors, correlation strength, and the Tony & Davies R (TDR) parameter.

HJD-245000	Velocity (kms^{-1})	V$_{err}$ (kms^{-1})	Corr. Height	TDR
7195.71288	-48.30	0.19	0.96	88.72
7195.75284	-48.07	0.20	0.96	88.86
7197.74781	-47.83	0.20	0.95	87.05
7200.77189	-48.18	0.18	0.94	95.28
7200.68975	-48.03	0.20	0.95	84.74
7200.72889	-48.01	0.18	0.95	95.87
7214.66610	-48.81	0.19	0.95	88.13
7214.70740	-48.65	0.20	0.95	85.08

Table 4.4: Radial velocity measurements using FXCOR for object **RGB.17278** along with errors, correlation strength, and the Tony & Davies R (TDR) parameter.

HJD-245000	Velocity (kms^{-1})	V$_{err}$ (kms^{-1})	Corr. Height	TDR
7195.75283	-48.92	0.23	0.92	74.79
7197.74780	-49.13	0.25	0.92	70.01
7200.72888	-49.22	0.23	0.91	71.41
7200.68975	-49.47	0.28	0.91	63.2

Table 4.5: Radial velocity measurements using FXCOR for object **RGB.17636** along with errors, correlation strength, and the Tony & Davies R (TDR) parameter.

HJD-245000	Velocity (kms^{-1})	V$_{err}$ (kms^{-1})	Corr. Height	TDR
7195.75283	-45.97	0.18	0.96	95.53
7197.74780	-45.49	0.19	0.95	91.61
7200.68974	-45.61	0.19	0.96	91.83
7200.72888	-45.92	0.17	0.95	100.41

Table 4.6: Radial velocity measurements using FXCOR for object **RGB.17671** along with errors, correlation strength, and the Tony & Davies R (TDR) parameter.

HJD-245000	Velocity (kms^{-1})	V$_{err}$ (kms^{-1})	Corr. Height	TDR
7195.71287	-41.96	0.18	0.94	97.13
7195.75282	-41.45	0.19	0.94	86.34
7197.74780	-39.67	0.18	0.95	94.82
7200.68974	-37.89	0.18	0.95	91.91
7200.72888	-38.18	0.17	0.93	101.17
7200.77188	-38.98	0.17	0.91	93.95
7214.66609	-32.74	0.19	0.93	89.93
7214.70739	-32.80	0.15	0.93	111.59

Table 4.7: Radial velocity measurements using FXCOR for object **RGB.17778** along with errors, correlation strength, and the Tony & Davies R (TDR) parameter.

HJD-245000	Velocity (kms^{-1})	V$_{err}$ (kms^{-1})	Corr. Height	TDR
7195.71287	-42.05	0.19	0.93	87.49
7200.77188	-42.10	0.17	0.92	102.88
7214.70739	-42.96	0.19	0.91	83.95
7214.66608	-42.64	0.17	0.9	91.06

Table 4.8: Radial velocity measurements using FXCOR for object **RGB.18045** along with errors, correlation strength, and the Tony & Davies R (TDR) parameter.

HJD-245000	Velocity (kms^{-1})	V$_{err}$ (kms^{-1})	Corr. Height	TDR
7195.75282	-48.26	0.17	0.96	102.26
7195.71286	-48.49	0.18	0.96	96.45
7197.74780	-48.49	0.17	0.96	97.55
7200.72887	-48.55	0.16	0.95	102.04
7200.68974	-48.66	0.19	0.96	98.14
7200.77188	-48.84	0.17	0.96	104.47
7214.66608	-49.08	0.20	0.94	83.74
7214.70738	-49.02	0.19	0.94	89.25

Table 4.9: Radial velocity measurements using FXCOR for object **RGB.18071** along with errors, correlation strength, and the Tony & Davies R (TDR) parameter.

HJD-245000	Velocity (kms^{-1})	V$_{err}$ (kms^{-1})	Corr. Height	TDR
7195.71286	-46.17	0.15	0.97	122.4
7195.75282	-46.47	0.17	0.96	107.07
7197.74780	-45.89	0.16	0.97	112.95
7200.72887	-46.32	0.16	0.96	109.05
7200.77188	-46.61	0.17	0.96	106.18
7200.68974	-45.87	0.15	0.97	121.89
7214.66608	-46.94	0.16	0.96	112.99
7214.70738	-47.16	0.16	0.95	111.34

Table 4.10: Radial velocity measurements using FXCOR for object **RGB.18535** along with errors, correlation strength, and the Tony & Davies R (TDR) parameter.

HJD-245000	Velocity (kms^{-1})	V_{err} (kms^{-1})	Corr. Height	TDR
7195.71286	-47.64	0.19	0.96	93.36
7195.75282	-47.04	0.19	0.96	89.31
7197.74779	-47.21	0.18	0.96	92.86
7200.72887	-47.00	0.18	0.96	91.57
7200.68973	-47.43	0.19	0.96	88.7
7200.77187	-47.70	0.18	0.95	95.06
7214.70738	-48.11	0.19	0.95	91.64
7214.66608	-48.27	0.21	0.95	79.88

Table 4.11: Radial velocity measurements using FXCOR for object **RGB.19104** along with errors, correlation strength, and the Tony & Davies R (TDR) parameter.

HJD-245000	Velocity (kms^{-1})	V_{err} (kms^{-1})	Corr. Height	TDR
7195.75281	-46.38	0.19	0.96	90.57
7197.74779	-45.98	0.19	0.96	91.35
7200.72886	-46.11	0.20	0.94	84.15
7200.68973	-46.11	0.19	0.96	88.79

Table 4.12: Radial velocity measurements using FXCOR for object **RGB.20213** along with errors, correlation strength, and the Tony & Davies R (TDR) parameter.

HJD-245000	Velocity (kms^{-1})	V_{err} (kms^{-1})	Corr. Height	TDR
7195.71284	-48.30	0.20	0.94	85.96
7200.77185	-47.13	0.20	0.94	82.94
7214.66606	-46.78	0.19	0.94	91.68
7214.70736	-46.81	0.20	0.95	82.84

Table 4.13: Radial velocity measurements using FXCOR for object **RGB.21185** along with errors, correlation strength, and the Tony & Davies R (TDR) parameter.

HJD-245000	Velocity (kms^{-1})	V_{err} (kms^{-1})	Corr. Height	TDR
7195.75279	-43.76	0.20	0.95	83.66
7195.71283	-43.40	0.19	0.96	93.37
7197.74777	-43.28	0.19	0.96	90.33
7200.77184	-43.87	0.19	0.94	90.18
7200.68971	-43.50	0.21	0.95	82.44
7200.72884	-43.64	0.18	0.95	95.5
7214.70735	-43.89	0.20	0.95	81.58
7214.66604	-44.09	0.19	0.94	86.13

Table 4.14: Radial velocity measurements using FXCOR for object **RGB.21350** along with errors, correlation strength, and the Tony & Davies R (TDR) parameter.

HJD-245000	Velocity (kms^{-1})	V$_{err}$ (kms^{-1})	Corr. Height	TDR
7195.75279	-45.65	0.19	0.95	90.38
7197.74776	-45.42	0.19	0.96	90.35
7200.68970	-45.58	0.19	0.96	91.01
7200.72884	-45.62	0.19	0.96	91.38

Table 4.15: Radial velocity measurements using FXCOR for object **RHB.15187** along with errors, correlation strength, and the Tony & Davies R (TDR) parameter.

HJD-245000	Velocity (kms^{-1})	V$_{err}$ (kms^{-1})	Corr. Height	TDR
7200.77191	-47.31	0.18	0.95	99.4
7200.68977	-47.76	0.22	0.96	80.49
7200.72890	-47.79	0.25	0.96	70.05
7214.66611	-47.95	0.22	0.96	75.59
7214.70742	-48.20	0.22	0.96	78.3

Table 4.16: Radial velocity measurements using FXCOR for object **RHB.21348** along with errors, correlation strength, and the Tony & Davies R (TDR) parameter.

HJD-245000	Velocity (kms^{-1})	V$_{err}$ (kms^{-1})	Corr. Height	TDR
7195.71283	-48.29	0.22	0.96	80.21
7195.75279	-48.65	0.19	0.96	88.84
7197.74776	-48.31	0.23	0.96	76.74
7200.77184	-48.28	0.21	0.96	82.37
7200.68970	-48.63	0.21	0.96	82.27
7200.72884	-48.46	0.23	0.96	76.86
7214.66604	-48.92	0.21	0.96	80.06

Figure 4.4: Radial velocity vs heliocentric julian day (HJD) for all the RGB stars. The time (x) axes have been shifted by 2450000 days, hence the axes are HJD–245000.

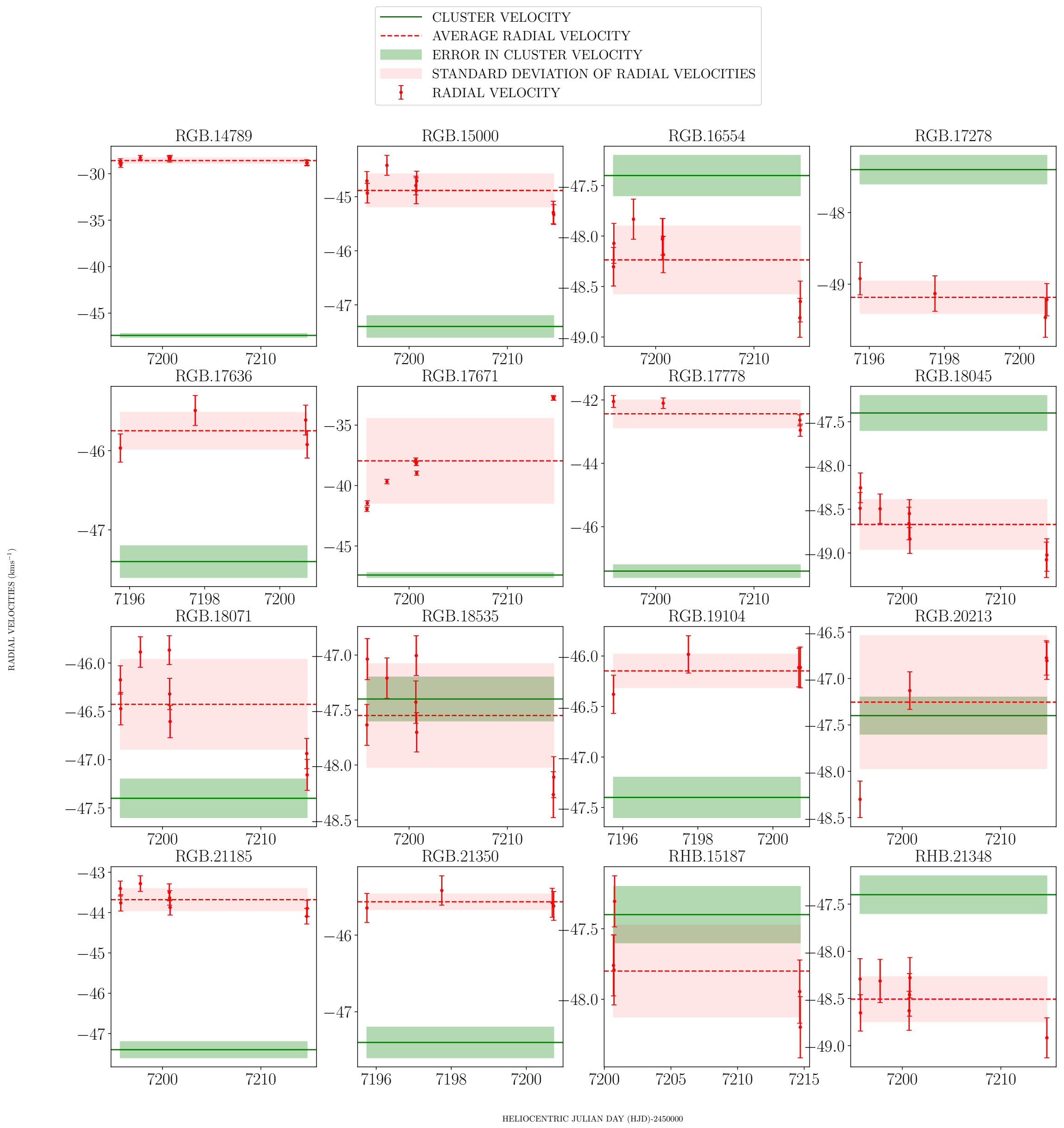

Figure 4.5: The radial velocity for all RGB stars.

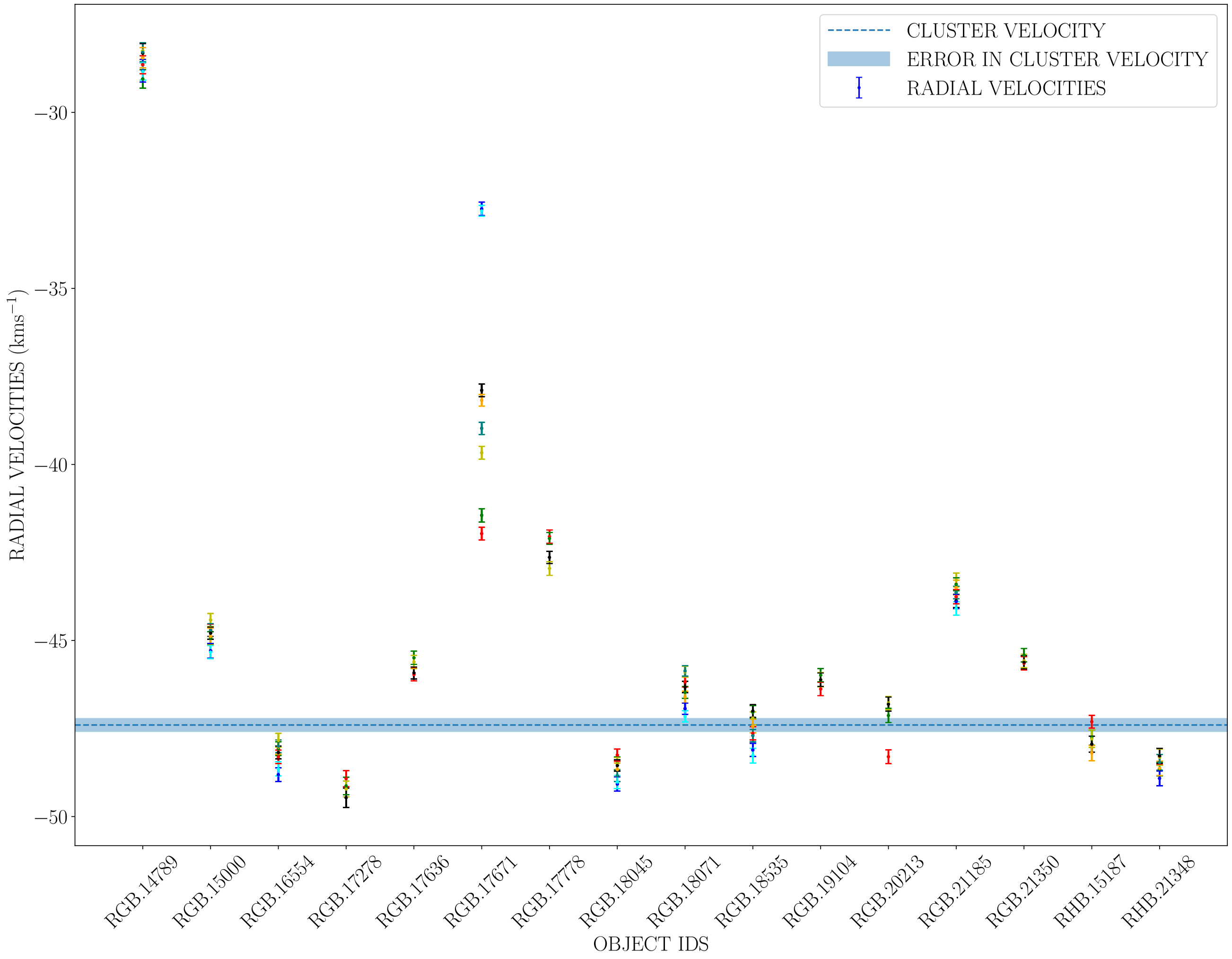

Figure 4.6: Radial velocity vs heliocentric julian day (HJD) for all the RGB stars from this work and also from Tofflemire et al. (2014). The time (x) axes have been shifted by 2450000 days, hence the axes are HJD–245000.

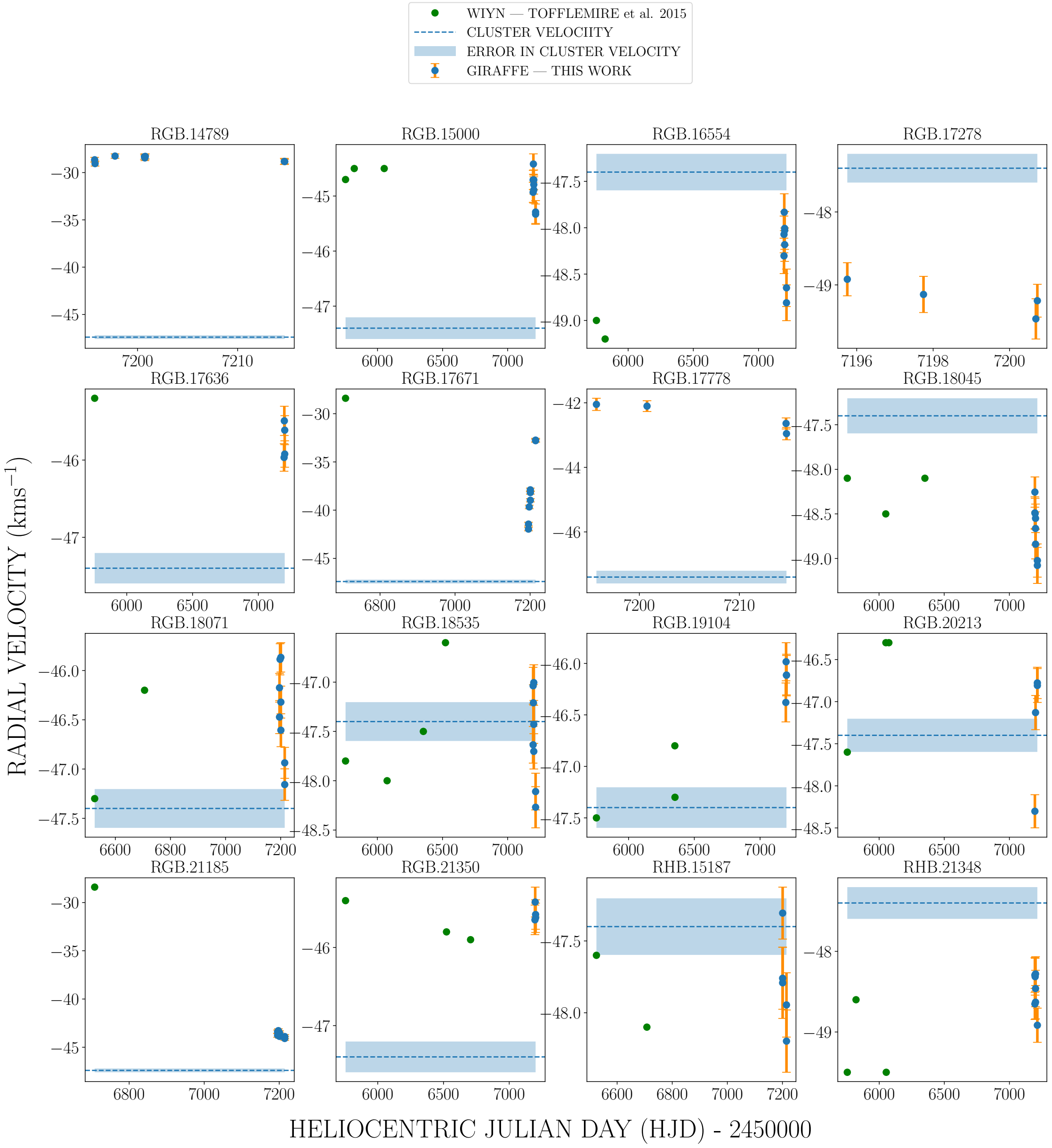

Table 4.17: Radial velocities of all objects from V$_1$ to V$_8$, average radial velocity (V$_{avg}$) , average of error in all radial velocities (V$_{err,\text{avg}}$), standard deviation in the radial velocities (σ_V) and the ratio of the standard deviation to the average RV errors (let's call it the Binary factor (Bf).

OBJECT ID	V$_1$	V$_2$	V$_3$	V$_4$	V$_5$	V$_6$	V$_7$	V$_8$	V$_{avg}$	V$_{err,\text{avg}}$	σ_V	Bf= σ_V/V$_{err,\text{avg}}$
RGB.14789	-28.65	-29.05	-28.25	-28.32	-28.45	-28.29	-28.82	-28.84	-28.58	0.27	0.30	1.11
RGB.15000	-44.71	-44.93	-44.42	-44.79	-44.89	-44.71	-45.29	-45.33	-44.88	0.19	0.31	1.63
RGB.16554	-48.30	-48.07	-47.83	-48.18	-48.03	-48.01	-48.81	-48.65	-48.24	0.19	0.34	1.79
RGB.17278	-48.92	-49.13	-49.22	-49.47	--	--	--	--	-49.18	0.24	0.22	0.92
RGB.17636	-45.97	-45.49	-45.61	-45.92	--	--	--	--	-45.75	0.18	0.23	1.28
RGB.17671	-41.96	-41.45	-39.67	-37.89	-38.18	-38.98	-32.74	-32.80	-37.96	0.18	3.51	19.50
RGB.17778	-42.05	-42.10	-42.96	-42.64	--	--	--	--	-42.44	0.18	0.44	2.44
RGB.18045	-48.26	-48.49	-48.49	-48.55	-48.66	-48.84	-49.08	-49.02	-48.67	0.18	0.29	1.61
RGB.18071	-46.17	-46.47	-45.89	-46.32	-46.61	-45.87	-46.94	-47.16	-46.43	0.16	0.46	2.88
RGB.18535	-47.64	-47.04	-47.21	-47.00	-47.43	-47.70	-48.11	-48.27	-47.55	0.19	0.47	2.47
RGB.19104	-46.38	-45.98	-46.11	-46.11	--	--	--	--	-46.15	0.19	0.17	0.89
RGB.20213	-48.30	-47.13	-46.78	-46.81	--	--	--	--	-47.25	0.20	0.72	3.60
RGB.21185	-43.76	-43.40	-43.28	-43.87	-43.50	-43.64	-43.89	-44.09	-43.68	0.19	0.27	1.42
RGB.21350	-45.65	-45.42	-45.58	-45.62	--	--	--	--	-45.57	0.19	0.10	0.53
RHB.15187	-47.31	-47.76	-47.79	-47.95	-48.20	--	--	--	-47.80	0.22	0.33	1.50
RHB.21348	-48.29	-48.65	-48.31	-48.28	-48.63	-48.46	-48.92	--	-48.51	0.21	0.24	1.14

¶ g here is in cgs units of cms^{-2}

5

Results

From the analysis in chapter 4, we have made multi-epoch radial velocity measurements of 16 RGB stars. We have listed individual velocity (RV) measurements along in tables 4.1 – 4.16, and table 4.17. These measurements all have close to unity correlation heights and high TDR parameter values that confirm the high strength and accuracy of our RV measurements. The cluster velocity (CV) for NGC 6791 in -47.40 ± 0.20 kms^{-1}(Tofflemire et al., 2014).

A star in a binary system would show changes in RV measurements unless the orbital plane of the star is face-on. As the angle of the orbital plane increase towards edge-on, the observed RV variations will keep on increasing in amplitude. On account of errors in our RV measurements there are variations in RVs for all stars. We need to distinguish the variations solely due to measurement error from variation due to binarity. We achieve this by establishing that the variation in the RVs is significant if the standard deviation in the RVs is at least twice the error in the RVs, that is if Bf>2. This is not a decisive condition, but only a necessary one. We will discuss the nature of RV variation by looking at all the RV curves of stars individually in figure 4.4, and further bringing into consideration figure 4.6 for more insights.

5.0.1 RGB.14789

The mean RV of this star is -28.60 ± 0.27 kms^{-1}, which is 18.80 kms^{-1}more than the CV. This would mean that the star is not a member of the open cluster NGC 6791. Nonetheless, the standard deviation in RV of this star is 0.30 kms^{-1}, whereas the average error in measurements is 0.27 kms^{-1}, resulting in Bf=1.11. Also on visually inspection of figure 4.4 all the RV measurements have error bars lying within the range of the standard deviation from the mean RV. Thus we can assert that the star has a insignificant RV variation to consider it as a binary candidate. This particular object did not have RV in the WIYN study.

5.0.2 RGB.15000

With a mean RV of -44.88 ± 0.19 kms^{-1}, it is within 3 kms^{-1}of the CV. We notice a velocity shift toward the mean cluster velocity with time, which could be a possible sign of binarity. But the Bf for this is 1.63, which means the standard deviation of the RVs is comparable to the RV errors. Also if we look at the combined RV curves, the WIYN RVs also appear to have a constant RV distribution. Hence, this star is quite unlikely to be a binary candidate.

5.0.3 RGB.16554

This star has a mean RV of -48.24 ± 0.19 kms^{-1}, which lies very close to the CV, within 1 kms^{-1}. With Bf of 1.79 , this star is at the borderline of our threshold but we do observe a trend going on in the RV curve. In the combined RV figure, we see WIYN RVs to be at lower RVs suggesting a variation. Nonetheless, on the basis of the Bf (<2) factor, we rule out this object as candidate for a binary and also on the lack of enough RV points to suggest a strong variation.

5.0.4 RBG.17278

The average RV -49.18 ± 0.24 kms^{-1}which is within 2 kms^{-1}of the cluster velocity. The Bf factor for this is 0.92 which indicates a strong consistency in the measured RVs. There aren't any WIYN RVs available for this object, and hence with the data at hand we rule out this star from being a binary candidate.

5.0.5 RGB.17636

With an average RV of -45.75 ± 0.18 kms^{-1}it is within 2 kms^{-1}of the cluster velocity. The Bf factor is 1.28 which suggests the same as a visual inspection of the RV curve does: a constant profile. The WIYN study for this star has one RV at -45.2 kms^{-1}. The variation in this point from the mean RV is 0.55 kms^{-1}, which falls insufficient of compelling us to consider it as a binary candidate.

5.0.6 RGB.17671

With an average RV of -37.96 ± 0.18 kms^{-1}, this star is within 10 kms^{-1}. The Bf factor for this star goes as high as 19.50. A clear trend is observed in the RVs as time evolves, where the RVs increase in a consistent fashion. The standard deviation is evidently larger than the errors in RVs, which suggesting the presence of a binary partner making it a very strong binary candidate. The WIYN study reports a single RV of -28.4 kms^{-1}which is beyond our RV measurements range of our study. This WIYN RV is present before all our RV measurements, with the next closest RV measurement from out study being at -41.96 kms^{-1}beyond which there is only a constant rise. This further implies that the RV has decreased between the WIYN RV and our earliest RV point. This variation is as high as 13.6 kms^{-1}. This object is our strongest candidate for a binary.

5.0.7 RGB.17778

RGB.17778 has a mean RV of -42.44 ± 0.18 kms^{-1}, within 5 kms^{-1}of the cluster velocity. The Bf factor is 2.44, greater than our threshold limit set at 2. The star is observed to have a decreasing RV in the data sample we have, and the Bf factor speaks for this variation. There are no WIYN RVs for this object, hence no data to corroborate our finding based on Bf. But we can certainly say there is a non-negligible probability of this star being in a binary system.

5.0.8 RGB.18045

With an average RV of -48.67 ± 0.18 kms^{-1}, it lies within 1 kms^{-1}of the cluster velocity. With a Bf factor of 1.61, it does not present a strong case for binarity. On considering the WIYN study for RVs of this star, we find values to be lying within the range of our RV data thus implying no significant deviation from the average RV. Hence we can safely assert that this star does not have a binary partner.

5.0.9 RGB.18071

The average RV calculated for this object is $-46.43{\pm}0.16$ kms^{-1}and it lies withing 1 kms^{-1}of CV. With a Bf of 2.88 this appears to be a strong candidate for a binary. There seems to be a certain anomaly in the radial velocity measurements at about HJD (245)7200 where there are three very different RVs within a short duration. Even if all the RVs that are present from each within a span of one day are averaged (assuming it as an anomaly and not an actual variation in RV), they yield a standard deviation of 0.48. This means a Bf factor of 3.00. This still corroborates with our earlier finding of Bf=2.88. Taking a look at the WIYN RVs shows two RVS, that show a considerable variation in the RVs within themselves as well. These WIYN RVs lie almost within the range of our mesaured RVs. Hence this star poses as a strong candidate for being present in a binary system.

5.0.10 RGB.18535

With an average RV of -47.55 ± 0.19 kms^{-1}, it lies within 0.2 kms^{-1}of the cluster velocity. The Bf factor is 2.47 which yet again makes it a strong candidate to be in a binary system just like the earlier case. Although there are disagreements between velocity measurements near HJD (245)7195 and (245)7200, the RV beyond HJD (245)7210 makes the case compelling. Following similar steps of averaging RVs that are in 1 day of vicinity yields a standard deviation of 0.44 and a Bf factor of 0.44/0/19=2.32. Again it supports the earlier conclusion with Bf=2.47. The WIYN RVs for this star provide an interesting sight. A clear variation in RVs can be noticed and one of the RVs also goes beyond the range of RVs derived by us. Hence, this star is a strong candidate to be in a binary system.

5.0.11 RGB.19104

The average velocity for this star is -46.15 ± 0.19 kms^{-1}and lies within 2 kms^{-1}of the cluster velocity. The Bf factor of 0.89 suggest a very monotonous nature of the RV curve. On the other hand, WIYN RVs provide some interesting RV data on this star. All the WIYN RVs lie beyond our range of measured RVs. There is a possibility Of this star being in a binary system since the WIYN RVs also cross the cluster velocity at some point. We give this star the status of uncertain where we can be sure of it's binarity were there error bars on WIYN RVs or atleast data from more epochs.

5.0.12 RGB.20213

This star has an average velocity of -47.25 ± 0.20 kms^{-1}, lying within 0.2 kms^{-1}of the cluster velocity. Without taking look at the Bf value, the R curve for this star presents a very compelling case for itself. The RVs are placed far out along the RV axis and shows a clear trend of increasing RV from below the CV to above it. The Bf factor is 3.60 and strongly presses on the binary nature of this star. The WIYN RVs show a similar find, where RVs are found below and above the cluster velocity. Two of these RVs are beyond the range of our measured RVs. Hence we attribute the status of a strong binary candidate to this star.

5.0.13 RGB.21185

The average RV of this star is -43.68 ± 0.19 kms^{-1}and finds itself within 4 kms^{-1}of the cluster velocity. The Bf factor is 1.42 that strongly suggests a constant RV for this object. The WIYN data poses a differing opinion with one RV measurement at -28.40 kms^{-1}. This shows a very different RV curve scenario such that we cannot eliminate the possibility of the star being in a binary system. We assign an uncertain status on its binarity where only more data on RVs would through light into the actual RV curve for this star.

5.0.14 RGB.21350

This star has an average velocity of -45.57 ± 0.19 kms^{-1}and it lies within 2 kms^{-1}of the cluster velocity. With a Bf factor of 0.53, the RV curve of this star is essentially flat. The WIYN RVs suggest similar observations where not much variation is observed within the RVs, and they lie almost within the range of RVs observed in this study. Hence there is no evident RV profile to suggest the presence of a binary partner for this star.

5.0.15 RHB.15187

With an average RV of -47.80 ± 0.22 kms^{-1}, it is within 0.5 kms^{-1}of the cluster velocity. The Bf factor for this star is 1.50, implying that the star almost has a constant RV profile. This is also supported by WIYN RV measurements as they lie within the range of our measured RVs. Hence this star does not exhibit binary nature.

5.0.16 RHB.21348

The average RV for this star is -48.51 ± 0.21 kms^{-1}and is present within 1.5 kms^{-1}of the cluster velocity. The Bf value for this star is 1.14 which strongly implies a constant RV profile as can also be seen in the RV curve. The WIYN RVs deviate slightly from our measured RVs. This could imply binarity but going by the trend of our measured RVs over a period of 20 days, no significant RV variation is observed. In the absence of enough RVs we can assert that there is less probability that this particular star is present in a binary system.

6

Conclusions

The strongest candidates we found to be in binary systems are as follows: RGB.17671, RGB. 17778, RGB.18071, RGB.18535, and RGB.20213. Hence there are about 5 very strong binary candidates found in the RGB sample we took from the open cluster NGC 6791. This conclusion is based on radial velocity measurements from this study which is complimented by radial velocities measured by Tofflemire et al. (2014). Recalling equation 1.3, the ratio of EHB to RC we had was,

$$\frac{\text{EHB}}{\text{RC}} = \frac{12}{45} = \frac{4}{15} = 0.267$$

,

and we expect to find a similar ratio between binaries and non-binaries in the RGBs. The ratio from our analysis of binary to non-binary RGBs is,

$$\frac{\text{Binaries in RGB}}{\text{Non-binaries in RGB}} = \frac{5}{10} = 0.5. \tag{6.1}$$

For decades there has been a constant debate over the formation mechanism of EHB stars in the open cluster NGC 6791, with competing research work going on in mass-loss and binarity as probable solutions. While the evolutionary path of mass loss would eventually form EHBs, it involves exaggerated mass-loss rates without concrete evidence for the occurrence of such heavy mass losses.

Carraro and Benvenuto (2017) used updated form of the Benvenuto and De Vito (2003) binary evolution code to demonstrate that EHBs can emerge from post common envelope of binary stars with masses agreeing to the cluster's turn-off ($M_{TO} \approx 1.15 M_{\odot}$). Our study compliments their work by finding probable binaries in the red giant branch. The masses of our RGB stars are $1.15 \pm 0.01 M_{\odot}$. While their work affirmed that binary stars can indeed form EHB stars, it is of extreme importance that these binary stars be detected. This in particular is not unexpected given a high binary percentage ($\sim 50\%$; Bedin et al. (2008); Twarog et al. (2011)) in NGC 6791.

The sample of stars employed by us are very small so we do not expect to get an exact ratio in equation 6.1 as we predicted in equation 1.3. What is important to note here is the qualitative aspect of this work. This is the first ever study dedicated to finding binary stars among the RGBs of NGC 6791. We have successfully shown that some RGB stars of the cluster can indeed exist in binary systems.

Owing to the availability of spectra only from ≤ 8 epochs for all our target stars, we could not get a multi/full phase radial velocity curve. Although RVs from Tofflemire et al. (2014) were useful, they were measured 3-4 years before our observations with the GIRAFFE. A future improvement to this work would be to obtain spectra of more red giants over more epochs (spanning at least 30 days) to be certain of the binary fraction in the red giant branch of the open cluster NGC 6791.

References

Alonso, A., Arribas, S., and Martínez-Roger, C. *Astronomy and Astrophysics, Supplement*, 140:261–277, 1999. doi: 10.1051/aas:1999521.

An, D., Pinsonneault, M. H., Terndrup, D. M., and Chung, C. *Astrophysical Journal*, 879 (2):81, Jul 2019. doi: 10.3847/1538-4357/ab23ed.

Bedin, L. R., King, I. R., Anderson, J., Piotto, G., Salaris, M., Cassisi, S., and Serenelli, A. *Astrophysical Journal*, 678:1279–1291, May 2008. doi: 10.1086/529370.

Benvenuto, O. G. and De Vito, M. A. *Monthly Notices of the Royal Astronomical Society*, 342(1):50–60, Jun 2003. doi: 10.1046/j.1365-8711.2003.06458.x.

Bertola, F., Capaccioli, M., and Oke, J. B. *Astrophysical Journal*, 254:494–499, March 1982. doi: 10.1086/159758.

Bressan, A., Marigo, P., Girardi, L., Salasnich, B., Dal Cero, C., Rubele, S., and Nanni, A. *Monthly Notices of the Royal Astronomical Society*, 427:127–145, November 2012. doi: 10.1111/j.1365-2966.2012.21948.x.

Brogaard, K., Vandenberg, D. A., Bruntt, H., Grundahl, F., Frandsen, S., Bedin, L. R., Milone, A. P., Dotter, A., Feiden, G. A., Stetson, P. B., Sandquist, E., Miglio, A., Stello, D., and Jessen-Hansen, J. *VizieR Online Data Catalog*, art. J/A+A/543/A106, 2012.

Buonanno, R., Caloi, V., Castellani, V., Corsi, C., Fusi Pecci, F., and Gratton, R. *Astronomy and Astrophysics, Supplement*, 66:79–109, 1986.

Buzzoni, A., Bertone, E., Carraro, G., and Buson, L. *Astrophysical Journal*, 749:35, April 2012. doi: 10.1088/0004-637X/749/1/35.

Carraro, G., Girardi, L., Bressan, A., and Chiosi, C. *Astronomy and Astrophysics*, 305:849, January 1996.

Carraro, G. and Benvenuto, O. G. *Astrophysical Journal, Letters*, 841(1):L10, May 2017. doi: 10.3847/2041-8213/aa7131.

Castellani, V., degl'Innocenti, S., and Pulone, L. *Astrophysical Journal*, 446:228, 1995. doi: 10.1086/175780.

Castelli, F. and Kurucz, R. L. volume 210 of *IAU Symposium*, page A20, January 2003.

Castelli, F., Gratton, R. G., and Kurucz, R. L. *Astronomy and Astrophysics*, 318:841–869, February 1997.

Chaboyer, B., Green, E. M., and Liebert, J. *Astronomical Journal*, 117(3):1360–1374, March 1999. doi: 10.1086/300794.

Code, A. D. and Welch, G. A. *Astrophysical Journal*, 256:1–12, May 1982. doi: 10.1086/159880.

Code, A. D. *Publications of the ASP*, 81(482):475, Oct 1969. doi: 10.1086/128809.

Dalessandro, E., Miocchi, P., Carraro, G., Jílková, L., and Moitinho, A. *Monthly Notices of the Royal Astronomical Society*, 449(2):1811–1818, May 2015. doi: 10.1093/mnras/stv395.

D'Cruz, N. L., Dorman, B., Rood, R. T., and O'Connell, R. W. *Astrophysical Journal*, 466: 359, July 1996. doi: 10.1086/177515.

Geisler, D., Villanova, S., Carraro, G., Pilachowski, C., Cummings, J., Johnson, C. I., and Bresolin, F. *Astrophysical Journal, Letters*, 756(2):L40, Sep 2012. doi: 10.1088/2041-8205/756/2/L40.

Gratton, R. G., Carretta, E., and Castelli, F. *Astronomy and Astrophysics*, 314:191–203, October 1996.

Greggio, L. and Renzini, A. *Astrophysical Journal*, 364:35, Nov 1990. doi: 10.1086/169384.

Jílková, L., Carraro, G., Jungwiert, B., and Minchev, I. *Astronomy and Astrophysics*, 541: A64, May 2012. doi: 10.1051/0004-6361/201117347.

Kalirai, J. S., Bergeron, P., Hansen, B. M. S., Kelson, D. D., Reitzel, D. B., Rich, R. M., and Richer, H. B. *The Astrophysical Journal*, 671(1):748–760, 2007. doi: 10.1086/521922. URL `https://doi.org/10.1086%2F521922`.

Kaluzny, J. and Rucinski, S. M. *Astronomy and Astrophysics, Supplement*, 114:1, Nov 1995.

Kaluzny, J. and Udalski, A. *Acta Astronomica*, 42:29–47, January 1992.

Kamann, S., Bastian, N. J., Gieles, M., Balbinot, E., and Hénault-Brunet, V. *Monthly Notices of the Royal Astronomical Society*, 483:2197–2206, 2019. doi: 10.1093/mnras/sty3144.

Kinman, T. D. *Astrophysical Journal*, 142:655, August 1965. doi: 10.1086/148329.

Koopmann, R. A., Lee, Y.-W., Demarque, P., and Howard, J. M. *Astrophysical Journal*, 423:380, March 1994. doi: 10.1086/173814.

Liebert, J., Saffer, R. A., and Green, E. M. *Astronomical Journal*, 107:1408, 1994. doi: 10.1086/116954.

Martinez-Medina, L. A., Gieles, M., Pichardo, B., and Peimbert, A. *Monthly Notices of the Royal Astronomical Society*, 474:32–44, February 2018. doi: 10.1093/mnras/stx2739.

Michaud, G., Bergeron, P., Wesemael, F., and Fontaine, G. *Astrophysical Journal*, 299: 741–744, December 1985. doi: 10.1086/163739.

Mochejska, B. J., Stanek, K. Z., and Kaluzny, J. *The Astronomical Journal*, 125(6):3175–3184, jun 2003. doi: 10.1086/374993. URL `https://doi.org/10.1086%2F374993`.

Pablo, H., Kawaler, S. D., and Green, E. M. *The Astrophysical Journal*, 740(2):L47, sep 2011. doi: 10.1088/2041-8205/740/2/l47. URL `https://doi.org/10.1088%2F2041-8205%2F740%2F2%2Fl47`.

Reimers, D. *Memoires of the Societe Royale des Sciences de Liege*, 8:369–382, Jan 1975.

Sneden, C. *Astrophysical Journal*, 184:839, September 1973. doi: 10.1086/152374.

Stetson, P. B., Bruntt, H., and Grundahl, F. *Publications of the Astronomical Society of the Pacific*, 115(806):413–447, 2003. doi: 10.1086/368337. URL `https://doi.org/10.1086%2F368337`.

Tofflemire, B. M., Gosnell, N. M., Mathieu, R. D., and Platais, I. *Astronomical Journal*, 148(4):61, October 2014. doi: 10.1088/0004-6256/148/4/61.

Twarog, B. A., Carraro, G., and Anthony-Twarog, B. J. *Astrophysical Journal, Letters*, 727: L7, January 2011. doi: 10.1088/2041-8205/727/1/L7.

van den Berg, M., Verbunt, F., Tagliaferri, G., Belloni, T., Bedin, L. R., and Platais, I. *The Astrophysical Journal*, 770(2):98, may 2013. doi: 10.1088/0004-637x/770/2/98. URL `https://doi.org/10.1088%2F0004-637x%2F770%2F2%2F98`.

van Loon, J., Boyer, M., Dupree, A., Evans, A., Gehrz, R., McDonald, I., and Woodward, C. Spitzer Proposal, March 2008.

Villanova, S., Carraro, G., Geisler, D., Monaco, L., and Assmann, P. *Astrophysical Journal*, 867(1):34, November 2018. doi: 10.3847/1538-4357/aae4e5.

Whitney, J. H., O'Connell, R. W., Rood, R. T., Dorman, B., Landsman, W. B., Cheng, K. P., Bohlin, R. C., Hintzen, P. M. N., Roberts, M. S., Smith, A. M., Smith, E. P., and Stecher, T. P. *Astronomical Journal*, 108:1350, 1994. doi: 10.1086/117157.

Yi, S. K. and Yoon, S.-J. *Astrophysics and Space Science*, 291:205–213, June 2004. doi: 10.1023/B:ASTR.0000044323.22830.35.

Yong, H., Demarque, P., and Yi, S. *The Astrophysical Journal*, 539(2):928–932, 2000. doi: 10.1086/309285. URL `https://doi.org/10.1086%2F309285`.

Acknowledgments

Every student is incomplete without a *Guru*. I would like to whole-heartedly thank Giovanni, my thesis supervisor, to have guided me ever so smoothly through this master thesis. He was available whenever I needed him, be it for a discussion or seeking some advice. Our connection goes way back before my master thesis even began. He had recommended me for an internship under Professor Chris Sneden at the University of Texas, Austin without which this thesis would have been impossible. I thank him for the opportunities he showered upon me, and I will forever be grateful to him for everything I have learned. His fun-loving character, friendly nature, and relaxed poise made it very easy to approach him for any problem whatsoever. May every student get a supervisor as amiable as mine.

Another set of *gurus*, who have been monumental in the making of this master thesis are Chris Sneden and Melike Afsar. My summer internship under them at UT Austin set the foundation for everything I have done in this thesis. In those two months, I learned a lot through the weekly discussions that they held just for me. I couldn‘t be more grateful for the skills they helped me develop in spectroscopy. They dedicated their time selflessly during busy schedules to solve my doubts and help me grow. Such people are rare, and I hope they prosper.

The two backbones of my life, my parents, have stood by every decision I have taken. The freedom they endowed upon me has helped me grow, become independent and brave to follow my heart. I am thankful for everything they have done for me and there is nothing more I could ever ask of them.

Life without friends is a life half-lived. In the last few years I have made some memorable friends: Hitesh, Mohammad, Divyanshu, Fu-Chi, Aishwarya, and Priyanka. Every discussion with them has been a fruitful one, be it related to astronomy or life. The philosophical arguments, life talks, and occasional dramas made this Astromundus experience with them

unforgettably worth it. I will always remember AstroMundus through this bunch of people.

It is the one who stays during difficult times, that makes it through with you in life. My fianceé, Namrata, has been that *one*. She has been there for me whenever I felt lonely, anxious, or lost. She has always motivated me to keep going and not give up. I respect her a lot and look up to her. Her way of life inspires me and I am grateful that she is a part of my life.